Reversible oxygen migration and phase transition in hafnia-based ferroelectric devices

Authors: Pavan Nukala[1,2*], Majid Ahmadi[1,3], Yingfen Wei[1,3], Sytze de Graaf[1], Evgenios Stylianidis[1,4], Tuhin Chakrabortty[2], Sylvia Matzen[5], Henny W. Zandbergen[6], Alexander Björling[7], Dan Mannix[8-10], Dina Carbone[7], Bart Kooi[1,3], Beatriz Noheda[1,3*]

Affiliations:

[1]Zernike Institute of Advanced Materials, University of Groningen, Groningen, 9747 AG, The Netherlands,

[2]Center for Nanoscience and Engineering, Indian Institute of Science, Bengaluru, 560012, India

[3]CogniGron (Groningen Cognitive Systems and Materials Center), University of Groningen, Nijenborgh NL-9747 AG Groningen, Netherlands.

[4]Department of Physics and Astronomy, University College London, Gower Street, London, WC1E 6BT, United Kingdom

[5]Center for Nanoscience and Nanotechnology, Paris-Saclay University, CNRS, 91120, Palaiseau, France

[6]Kavli Institute of Nanoscience, Faculty of Applied Sciences, Delft University of Technology, 2628 CJDelft, The Netherlands

[7] MAX IV Laboratory, Lund University, 22100 Lund, Sweden

[8] University Grenoble Alpes, CNRS, Institut Néel, 38042 Grenoble, France

[9]European Spallation Source, SE-221 00 Lund, Sweden.

[10]Aarhus University, Langelandsgade 140, DK-8000 Aarhus, Denmark.

*Correspondence to: pnukala@iisc.ac.in, b.noheda@rug.nl

Abstract:

Unconventional ferroelectricity exhibited by hafnia-based thin films, robust at nanoscale sizes, presents tremendous opportunities in nanoelectronics. However, the exact nature of polarization switching remains controversial. We investigated $La_{0.67}Sr_{0.33}MnO_3/Hf_{0.5}Zr_{0.5}O_2$ capacitor interfaced with various top electrodes while in situ electrical biasing using atomic resolution microscopy with direct oxygen imaging, as well as synchrotron nanobeam diffraction. When the top electrode is oxygen reactive, we clearly show reversible oxygen vacancy migration with electrodes being the source and sink of oxygen, and the dielectric layer acting as a fast conduit at millisecond timescales. With non-reactive top electrodes and at longer time scales (seconds), the dielectric layer also acts as an oxygen source/sink. Our results show that ferroelectricity in hafnia-based thin films is unmistakably intertwined to oxygen voltammetry.

Main Text:

The discovery of silicon compatible nano-ferroelectricity in hafnia-based thin films (*1*) has triggered a vast amount of fundamental research and rejuvenated interest in ferroelectric materials in microelectronics, for low-power non-volatile memory and logic devices. This ferroelectricity is

robust even at film thicknesses as low as 1 nm (*2–4*), a situation that was believed impossible based on the classical understanding of ferroelectricity. The spontaneous polarization observed in these films is ascribed generally to a metastable polar orthorhombic phase (*Pca2$_1$*, o-phase) (*5*). A higher energy rhombohedral phase (*R3m/R3*, r-phase) has been reported for epitaxial growth of $Hf_{0.5}Zr_{0.5}O_2$ (HZO) on $La_{0.67}Sr_{0.33}MnO_3$ (LSMO) buffered perovskite and on trigonal substrates (*6*). Remnant polarization (P_r) values as high as 35 $\mu C/cm^2$ were measured (*7*) on HZO. The pronounced effects of particle size reduction, surface effects, dopants, oxygen vacancies ($\ddot{V}_o$), epitaxial strain and residual stresses at nanoscale have been investigated as possible reasons to stabilize these otherwise metastable phases in thin films (*5*, *8*, *9*). On the other end of the size range, films as thick as 1 μm (*10*) and bulk samples (*11*) are ferroelectric, with the stabilization due to dopant and defect chemistry (*10*, *12*).

Armed with an understanding of the virgin state polarization, vibrant research is being conducted on the mechanism of polarization switching. The dynamics of this process, through the lens of a nucleation-limited switching model and pointing out the negligible role of domain growth (or domain wall motion), have been studied for doped hafnia films grown in the o-phase (*13–19*). Flat phonon bands and localized dipoles in half unit cells in the o-phase have been postulated as an intrinsic reason for switching without forming domain walls in these systems (*20*).

Hafnia-based and zirconia-based materials are also an important class of resistive memory devices and oxygen conductors that exhibit memristive hysteresis driven by $\ddot{V}_o$ conduction and redox reactions (*21*, *22*). More generally, in devices of thin-film ferroelectric oxides such as tunnel junctions, both $\ddot{V}_o$ migration and polarization switching lead to hysteresis (*23–28*). Understanding whether these effects are synergetic or independent is crucial to achieve device control(*29–33*). In tunnel junctions of HZO thin-films on LSMO buffered $SrTiO_3$ (STO), Wei et al. (*23*) observed a divergence of the tunnel electro-resistance (TER), from 100% to 10^6 % upon device cycling, which the authors explained as a possible transition from polarization switching to $\ddot{V}_o$ migration assisted switching. This observation suggested the two mechanisms are independent. Sulzbach et al. (*24*) also reported a similar divergence in the TER as a function of the applied voltage in HZO layers before breakdown. However, the electric polarization in hafnia has been theoretically proposed to originate from oxygen vacancies through electrostrictive effects, strongly suggesting the extrinsic nature of the polarization switching (*29*). Direct structural observations during polarization switching can potentially resolve these controversies (*34*).

We report operando atomic scale electron microscopy investigations of LSMO/HZO/LSMO capacitor stacks grown on conducting (Nb-doped) STO substrate under electric field ((*35*)). LSMO is a standard choice of bottom electrode in complex oxide devices (*23–26*,*31*) and so our conclusions are relevant for understanding a wider class of devices. We performed in situ biasing measurements while employing two scanning transmission electron microscopy (STEM) imaging modes, high-angle annular dark-field (HAADF) STEM and integrated differential phase contrast (iDPC) STEM. With iDPC STEM, we recently imaged hydrogen atoms next to Ti metal atoms (*36*), demonstrating this robust atomic resolution imaging technique for simultaneously measuring heavy and light elements. By directly imaging oxygen, we provide evidence of the reversible and hysteretic migration of $\ddot{V}_o$ from the bottom to the top electrode through the HZO layer. Associated with such migration, we show $\ddot{V}_o$ induced phase transitions in LSMO (bottom electrode) and HZO layers. Additionally, through operando x-ray diffraction, ex situ microscopy, and transport

measurements on devices with both noble (Au) and oxygen reactive top electrodes (LSMO, TiN), we show that oxygen voltammetry is also found at short timescales (millisecond and less). We believe these observations clearly show that polarization switching and oxygen voltammetry are not independent. The long-term effects include redox-based and topotactic phase transitions in both HZO and LSMO layers.

We begin by showing the evolution of the epitaxial LSMO layer (bottom electrode) with bias, with the voltage applied to the top electrode, and keeping the bottom electrode at 0 V (Fig. S1, 22). Our iDPC-STEM image of the virgin state (Fig. 1A, Fig. S2A) shows the antiphase octahedral δ tilts present in the LSMO perovskite structure (22). Mn-O-Mn bond angles, as we measured in various s regions, are between 165°-176° (*37*). Upon increasing the bias to 2 V, a noticeable displacement of Mn columns away from the center of oxygen octahedra (Fig. 1B) appears throughout the film (barring the first three monolayers at the interface with Nb:STO). These displacements are randomly oriented with a mean value of 18.6 pm and std. deviation of 10.2 pm (Fig S3), indicating a transformation from an MnO_6 octahedral towards an MnO_5 square pyramidal coordination ((*35*)). Thus, at 2 V the LSMO film contains a combination of MnO_5 and MnO_6 polyhedra. While this structural feature was not previously observed for LSMO, Brownmillerite (BM, oxygen deficient perovskite) phases are reported to exhibit MnO_5 square pyramids in the parent compound, $SrMnO_3$ (*38*). We refer to this MnO_5 - MnO_6 combination as a BM-precursor phase (*39*). As for the first 3 monolayers, an important feature is the exaggerated antiphase δ tilts, with Mn-O-Mn bond angles of 143-146° that are not typical of perovskite structures (Fig. S2B-D).

Upon increasing the biasing voltage to 4 V, LSMO converts into a well-studied BM phase (*37*,*38*) except for the first few monolayers near the interface with the substrate, which transform to the BM-precursor phase (Fig. S4A). Transformation from perovskite to BM phase occurs via $\ddot{V}_o$ ordering in every alternate Mn-O plane along the *c'*-axis (Fig. 1C), transforming the Mn coordination from octahedral or square pyramidal to tetrahedral. Back-to-back MnO_4 tetrahedra along [1-10] alternate with MnO_6 octahedra along *c*', indicating the BM phase (Fig. 1C). This transformation is hysteretic and non-volatile, with LSMO remaining in the BM phase even when the external bias is removed (Fig. S4, (*35*)).

The multiple-step transformations (Fig. 1D) from MnO_6 octahedra (virgin state) towards square pyramids plus octahedra (2 V), to alternating octahedra and tetrahedra (4 V) also correlate to the variation of the pseudo-cubic lattice parameter along the electric-field direction (called *c'*). We determined the *c'* values at various bias voltages for the first 20 monolayers in LSMO starting from the Nb:STO interface (Fig. 1E). In the virgin state, we measured *c'* to be 384 (± 5) pm with $\ddot{V}_o$ disorder induced expansion in some planes (*35*). At 2 V, *c'* oscillates with values between 335 and 425 pm, without resulting in any particular superstructure. At 4 V, except for the first few monolayers, *c'* alternates between 375 and 445 pm, doubling the lattice periodicity. Energy dispersive spectroscopy (*35*) reveals a clear gradient of oxygen concentration in the bottom electrode, compared to the virgin state, even at a low bias of 1.5 V, with more $\ddot{V}_o$ occurring closer to the Nb:STO interface (Fig. 1F,G).

Importantly, the BM phase can be reoxygenated when negative voltages are applied to the top electrode. We show this takes place for biases as low as -1 V (Fig. S5A). The hysteretic BM phase clearly begins to reoxygenate in iDPC-STEM images of the same field view at 0 V and -1.3 V

(Fig. 2A-B), with the appearance of extra oxygen columns at -1.3 V in the Mn-O planes that were oxygen deficient at 0 V (Fig. S5A). Upon ramping the bias to -3 V, the entire layer converts to the BM-precursor phase (Fig. 2C) and was retained also when the bias is removed (Fig. 2D), as we confirmed by the corresponding 'disorderly' *c'* variation (Fig. S5B).

In order to address the timescales of the processes associated with de- and re-oxygenation of LSMO layers, we followed the dynamics through HAADF-STEM image acquisition, after poling at -4 V (transforming LSMO completely back to the starting perovskite phase). In the HAADF-STEM image evolution that occurs within 2 minutes of one region having a bias increase to 3V (Fig. 2E), the initial perovskite phase changes to the BM-precursor phase in 60 seconds, and then to the BM phase within 120 seconds. These changes were indicated by the variations we observed in the *c'* parameter. By applying -3 V, we observed a complete transformation from a BM phase back to perovskite phase within 90 seconds in the region (Fig. 2F, FFT in Fig. S5C). We then followed the same region for 10 second using a faster HAADF-STEM image series (1.2 seconds/frame). From the *c'* parameter variations, we concluded that the BM-precursor phase transformed to the perovskite phase (Fig. 2F, center panel). Thus, while the complete transformation from perovskite to BM and back takes about a couple of minutes at 3 and -3 V, $\ddot{V}_o$ migration and partial phase-transitions already started occurring in time scales of seconds at these voltages. At 2 V, however, the partial transition to the BM-precursor phase itself takes 3-4 hours. The change in kinetics with voltage is consistent with the ultra non-linear "voltage-time dilemma" typically observed in oxide resistive memories (*42*). Thus, we expect that at higher voltages these mechanisms will occur at very short time scales.

We also monitored the structural evolution in the HZO (6 nm) layer under the application of bias. From the multislice iDPC-STEM image simulations for HZO (see also Ref. (*43*)) in the r-phase (*R3m*) with [111] out-of-plane (Fig. 3A, inset), we recognized the (001) planes (at ~55^o with respect to the [111] direction) by cationic (Hf/Zr) columns surrounded by two oxygen columns on either side of them. In the virgin state, our experimental images perfectly match the r-phase simulations. We followed the evolution of a supercell (Fig. 3A) in this grain upon application of bias along the out of plane [111] direction. We show how the displacement of $\ddot{V}_o$ for this supercell occurs ((*35*), Fig S6A) with respect to the 0 V configuration (Fig. 3B). While $\ddot{V}_o$ migrate towards the bottom electrode with increasing bias (Fig. 3B), they also gather some in-plane displacement (Fig 3B, inset).

At 4 V, the same grain transforms into a combination of multiple grains (Fig. 3C). Upon inspecting various regions in the film, we found that the majority of the grains have changed their structure from r-phase towards the more thermodynamically stable orthorhombic (o-) and monoclinic (m-) phases (Fig. 3D, Fig. S6C). The o-phase is commonly observed in ferroelectric HZO layers grown by various methods (*5*), while the r-phase is only observed under specific growth procedures and conditions (*6*). Our observations on HZO point to the r-phase being stabilized under slight oxygen deficient conditions. Replenishment of oxygen in the HZO layer under bias (originating from the bottom LSMO layer), transforms it into more stoichiometric m- or o-phases. The $\ddot{V}_o$ in the HZO layer, and thus the r-phase, is restored (by reverse migration) upon applying a bias of -3 V, as can be seen from the perfect match of the experimental iDPC-STEM of two representative domains (180^o rotated from each other) (Fig. 3E), with the multislice image simulations (Fig. 3A, inset).The m/o-phases can be reversibly obtained again in subsequent cycles of positive bias (Fig S6D).

To elucidate the effects of device cycling with sub-millisecond pulses (*35*), we present results on tunnel junction Co/HZO (2 nm)/LSMO//STO devices switched between low-resistance state (LRS) and high-resistance state (HRS) at large voltages of ±6 V. The devices showed an increasing TER (*35*) from 100% (stage A) to 10^6 % (stage B) upon cycling ~100 times (*23*, *44*) . An iDPC-STEM image from a selected region in the LSMO (bottom electrode) layer in the LRS (stage A) (Fig. 4A) shows a clear perovskite structure. In the HRS (stage B), however (Fig. 4B), Co inhomogeneously oxidizes exhibiting co-existing Co rich and CoO_x rich regions as revealed from the EDS analysis (Fig S7). This leaves oxygen deficient LSMO in the BM precursor-phase. Thus, progression from stage A to stage B results in gradual increase of CoO_x regions, an accumulated effect of oxygen voltammetry, which is reflected electrically in diverging resistance values.

To disentangle the short-term field effects on our devices from accumulated effects (*35*), we report ex situ structure-property correlation results on ferroelectric capacitor stacks of LSMO (or TiN)/HZO (7 nm)/LSMO//STO cycled at 1kHz for <10 times at 5.5 V. The intrinsic P_r of our virgin devices in r-phase obtained from atomic displacements ((*35*), Fig S5B) is < 9 μC/cm^2, which is very small compared to the 35 μC/cm^2 that were measured from P-V loops at room temperature (*7*). This discrepancy is already an indication that most of the switching charge is intertwined with extrinsic factors. From the P-V hysteresis loops at various temperatures (Fig. 4C), we observed that, contrary to what it is expected in classical ferroelectrics, the P_r increases with increasing temperature in the range from 150 K to 300 K (*22*). This observation is in line with the polarization switching being correlated to the thermally activated oxygen migration mechanism. These devices were prepared in a “down polarized” configuration (5.5 V,1 kHz) and imaged. The iDPC-STEM images clearly reveal the oxygen deficient BM-precursor phase in the bottom LSMO layer close to the HZO interface (Fig. 4D) as also confirmed by corresponding disorderly oscillations in the *c’* parameter (Fig. 4D, inset). Close to the STO interface, we found exaggerated oxygen octahedral tilts with Mn-O-Mn bond angles < 146^o (marked in Fig S8A), which is the same interfacial feature observed during in situ DC testing at 2 V (Fig. S2B). These observations also suggest that such extreme tilts initiate the transformation from perovskite to BM-precursor phase. These incipient oxygen-migration induced topotactic structural transitions result from the discharge of $\ddot{V}_o$ in the electrodes. This thermally activated process leads to a built-in field at lower temperature, which decreases as the temperature rises (Fig. S8B,C). The HZO layer, however, remains in an r-phase (Fig 4E), revealing that it just acts as a conduit of oxygen between the source and sink (both reactive) electrodes in the short-term.

We conducted comparative operando synchrotron nanobeam diffraction on Au/HZO/LSMO and LSMO/HZO/LSMO capacitors in order to answer the question whether oxygen voltammetry can still occur if HZO is interfaced with a non-reactive electrode in the short-term ((*35*), Fig S9). . Both devices showed ferroelectric switching peaks (Fig. 4E, Fig. S10) and we cycled them at 100 Hz in a modest voltage range between -3.5 and 3.5 V for tens of thousands of cycles (Fig S10C). In LSMO/HZO/LSMO devices the virgin state and cycled state do not show any substantial differences of the HZO lattice parameter, indicating the persistence of the r-phase during cycling (Fig. S10D). However, in the case of Au/HZO/LSMO, we see evidence that a monoclinic phase (with a Bragg peak at 2θ=24.9^o) appears after cycling, and coexists with the r-phase (Fig S10E,F). This reveals that the HZO layer itself is forced to act as source/sink of oxygen vacancies in the short-term (*35*), when Au is used as a top electrode, resulting in reversible structural phase

transitions between r and m phases. Further DC biasing, results in increase of m-phase fraction increasing positive bias, in agreement with the long-term in situ TEM observations (Fig S11).

Using the model system of epitaxial HZO/LSMO/STO, we demonstrated that oxygen voltammetry and ferroelectric switching are intertwined (Fig 4F, (*35*)).With reactive top electrodes such as TiN (*45*), Co, and LSMO, the HZO layer acts as a mere conduit for reversible oxygen migration between the electrodes, with incipient topotactic transformations taking place in them. With a noble top electrode (Au), HZO instead itself acts as a sink/source of $\ddot{V}_o$. In the longer-term, redox-based phase-transition effects that follow oxygen migration in both HZO and LSMO become more dramatic. We clearly show that oxygen voltammetry is intertwined with ferroelectric switching of HZO. While we remain agnostic about the nature of this coupling, recent predictions of electrochemical origin of ferroelectricity in hafnia-based compounds (*29*), as well as demonstrations of giant electrostriction in the sister compound Gd:CeO_2, (*46*) can provide important clues.

In the context of tunnel junction devices, perovskite manganites (*47*) are routinely used as a back electrodes (*24–27*, *48*). Their crucial role as oxygen conducting memristive layers (*41*) actively participating in charge transport is being recognized (*35*), with recent seminal demonstrations in ferroelectric tunnel junctions (*28*). Thus, our results have deep implications not just to hafnia-based ferroelectrics, but also to the wider field of oxide electronics.

References and Notes:

1. T. S. Böscke, J. Müller, D. Bräuhaus, U. Schröder, U. Böttger, Ferroelectricity in hafnium oxide thin films. *Appl. Phys. Lett.* (2011), doi:10.1063/1.3634052.

2. A. Chernikova, M. Kozodaev, A. Markeev, D. Negrov, M. Spiridonov, S. Zarubin, O. Bak, P. Buragohain, H. Lu, E. Suvorova, A. Gruverman, A. Zenkevich, Ultrathin $Hf_{0.5}Zr_{0.5}O_2$ Ferroelectric Films on Si. *ACS Appl. Mater. Interfaces* (2016), doi:10.1021/acsami.5b11653.

3. X. Tian, S. Shibayama, T. Nishimura, T. Yajima, S. Migita, A. Toriumi, Evolution of ferroelectric HfO_2 in ultrathin region down to 3 nm. *Appl. Phys. Lett.* (2018), doi:10.1063/1.5017094.

4. S. S. Cheema, D. Kwon, N. Shanker, R. dos Reis, S.-L. Hsu, J. Xiao, H. Zhang, R. Wagner, A. Datar, M. R. McCarter, C. R. Serrao, A. K. Yadav, G. Karbasian, C.-H. Hsu, A. J. Tan, L.-C. Wang, V. Thakare, X. Zhang, A. Mehta, E. Karapetrova, R. V Chopdekar, P. Shafer, E. Arenholz, C. Hu, R. Proksch, R. Ramesh, J. Ciston, S. Salahuddin, Enhanced ferroelectricity in ultrathin films grown directly on silicon. *Nature*. **580**, 478–482 (2020).

5. U. Schröder, C. S. Hwang, H. Funakubo, Eds., *Ferroelectricity in doped hafnium oxide* (Woodhead Publishing 2019, ed. 1st).

6. P. Nukala, Y. Wei, V. de Haas, J. Antoja-Lleonart, Q. Guo, B. Noheda, Guidelines for the stabilization of a polar rhombohedral phase in epitaxial $Hf_{0.5}Zr_{0.5}O_2$ thin films. *arXiv:2005.01809* (2020).

7. Y. Wei, P. Nukala, M. Salverda, S. Matzen, H. J. Zhao, J. Momand, A. S. Everhardt, G. Agnus, G. R. Blake, P. Lecoeur, B. J. Kooi, J. Íñiguez, B. Dkhil, B. Noheda, A

rhombohedral ferroelectric phase in epitaxially strained $Hf_{0.5}Zr_{0.5}O_2$ thin films. *Nat. Mater.* (2018), doi:10.1038/s41563-018-0196-0.

8. R. Materlik, C. Kunneth, A. Kersch, The origin of ferroelectricity in $Hf_{1-x}Zr_xO_2$: A computational investigation and a surface energy model. *J. Appl. Phys.* (2015), doi:10.1063/1.4916707.

9. S. J. Kim, J. Mohan, S. R. Summerfelt, J. Kim, Ferroelectric $Hf_{0.5}Zr_{0.5}O_2$ Thin Films: A Review of Recent Advances. *JOM* (2019), , doi:10.1007/s11837-018-3140-5.

10. T. Mimura, T. Shimizu, H. Funakubo, Ferroelectricity in $YO_{1.5}$-HfO_2 films around 1 μ m in thickness. *Appl. Phys. Lett.* (2019), doi:10.1063/1.5097880.

11. X. Xu, F.-T. Huang, Y. Qi, S. Singh, K. M. Rabe, D. Obeysekera, J. Yang, M.-W. Chu, S.-W. Cheong, Kinetically stabilized ferroelectricity in bulk single-crystalline HfO2:Y. *Nat. Mater.* (2021), doi:10.1038/s41563-020-00897-x.

12. Y. Zhou, Y. K. Zhang, Q. Yang, J. Jiang, P. Fan, M. Liao, Y. C. Zhou, The effects of oxygen vacancies on ferroelectric phase transition of HfO_2-based thin film from first-principle. *Comput. Mater. Sci.* (2019), doi:10.1016/j.commatsci.2019.05.041.

13. H. Mulaos, J. O. Ker, S. Mulle, U. Schroeder, J. Müller, P. Polakowski, S. Flachowsky, R. Van Bentum, T. Mikolajick, S. Slesazeck, Switching kinetics in nanoscale hafnium oxide based ferroelectric field-effect transistors. *ACS Appl. Mater. Interfaces* (2017), doi:10.1021/acsami.6b13866.

14. M. Pešić, C. Künneth, M. Hoffmann, H. Mulaosmanovic, S. Müller, E. T. Breyer, U. Schroeder, A. Kersch, T. Mikolajick, S. Slesazeck, A computational study of hafnia-based ferroelectric memories: from ab initio via physical modeling to circuit models of ferroelectric device. *J. Comput. Electron.* (2017), doi:10.1007/s10825-017-1053-0.

15. N. Gong, X. Sun, H. Jiang, K. S. Chang-Liao, Q. Xia, T. P. Ma, Nucleation limited switching (NLS) model for HfO_2-based metal-ferroelectric-metal (MFM) capacitors: Switching kinetics and retention characteristics. *Appl. Phys. Lett.* (2018), doi:10.1063/1.5010207.

16. P. Buragohain, C. Richter, T. Schenk, H. Lu, T. Mikolajick, U. Schroeder, A. Gruverman, Nanoscopic studies of domain structure dynamics in ferroelectric La:HfO_2 capacitors. *Appl. Phys. Lett.* (2018), doi:10.1063/1.5030562.

17. S. Migita, H. Ota, H. Yamada, K. Shibuya, A. Sawa, A. Toriumi, Polarization switching behavior of Hf-Zr-O ferroelectric ultrathin films studied through coercive field characteristics *Japanese Journal of Applied Physics* (2018), doi: 10.7567/JJAP.57.04FB01.

18. Y. H. Lee, S. D. Hyun, H. J. Kim, J. S. Kim, C. Yoo, T. Moon, K. Do Kim, H. W. Park, Y. Bin Lee, B. S. Kim, J. Roh, M. H. Park, C. S. Hwang, Nucleation-Limited Ferroelectric Orthorhombic Phase Formation in $Hf_{0.5}Zr_{0.5}O_2$ Thin Films. *Adv. Electron. Mater.* (2019), doi:10.1002/aelm.201800436.

19. T. Schenk, M. Hoffmann, J. Ocker, M. Pešić, T. Mikolajick, U. Schroeder, Complex internal bias fields in ferroelectric hafnium oxide. *ACS Appl. Mater. Interfaces* (2015), doi:10.1021/acsami.5b05773.

20. H.-J. Lee, M. Lee, K. Lee, J. Jo, H. Yang, Y. Kim, S. C. Chae, U. Waghmare, J. H. Lee, Scale-free ferroelectricity induced by flat phonon bands in HfO_2. *Science (80-.).* (2020), doi:10.1126/science.aba0067.

21. C. Li, Y. Yao, X. Shen, Y. Wang, J. Li, C. Gu, R. Yu, Q. Liu, M. Liu, Dynamic observation of oxygen vacancies in hafnia layer by in situ transmission electron microscopy. *Nano Res.* (2015), doi:10.1007/s12274-015-0857-0.

22. S. U. Sharath, S. Vogel, L. Molina-Luna, E. Hildebrandt, C. Wenger, J. Kurian, M. Duerrschnabel, T. Niermann, G. Niu, P. Calka, M. Lehmann, H. J. Kleebe, T. Schroeder, L. Alff, Control of Switching Modes and Conductance Quantization in Oxygen Engineered HfO_x based Memristive Devices. *Adv. Funct. Mater.* (2017), doi:10.1002/adfm.201700432.

23. Y. Wei, S. Matzen, C. P. Quinteros, T. Maroutian, G. Agnus, P. Lecoeur, B. Noheda, Magneto-ionic control of spin polarization in multiferroic tunnel junctions. *npj Quantum Mater.* (2019), doi:10.1038/s41535-019-0201-0.

24. M. C. Sulzbach, S. Estandía, X. Long, J. Lyu, N. Dix, J. Gàzquez, M. F. Chisholm, F. Sánchez, I. Fina, J. Fontcuberta, Unraveling Ferroelectric Polarization and Ionic Contributions to Electroresistance in Epitaxial $Hf_{0.5}Zr_{0.5}O_2$ Tunnel Junctions. *Adv. Electron. Mater.* (2020), doi:10.1002/aelm.201900852.

25. M. Hambe, A. Petraru, N. A. Pertsev, P. Munroe, V. Nagarajan, H. Kohlstedt, Crossing an interface: Ferroelectric control of tunnel currents in magnetic complex oxide heterostructures. *Adv. Funct. Mater.* (2010), doi:10.1002/adfm.201000265.

26. D. Pantel, S. Goetze, D. Hesse, M. Alexe, Room-temperature ferroelectric resistive switching in ultrathin Pb(Zr 0.2Ti0.8)O_3 films, *ACS Nano* (2011), doi: 10.1021/nn2018528.

27. S. Boyn, J. Grollier, G. Lecerf, B. Xu, N. Locatelli, S. Fusil, S. Girod, C. Carrétéro, K. Garcia, S. Xavier, J. Tomas, L. Bellaiche, M. Bibes, A. Barthélémy, S. Saïghi, V. Garcia, Learning through ferroelectric domain dynamics in solid-state synapses. *Nat. Commun.* (2017), doi:10.1038/ncomms14736.

28. V. Rouco, R. El Hage, A. Sander, J. Grandal, K. Seurre, X. Palermo, J. Briatico, S. Collin, J. Trastoy, K. Bouzehouane, A. I. Buzdin, G. Singh, N. Bergeal, C. Feuillet-Palma, J. Lesueur, C. Leon, M. Varela, J. Santamaría, J. E. Villegas, Quasiparticle tunnel electroresistance in superconducting junctions. *Nat. Commun.* (2020), doi:10.1038/s41467-020-14379-w.

29. V. Mikheev, A. Chouprik, Y. Lebedinskii, S. Zarubin, Y. Matveyev, E. Kondratyuk, M. G. Kozodaev, A. M. Markeev, A. Zenkevich, D. Negrov, Ferroelectric Second-Order Memristor. *ACS Appl. Mater. Interfaces* (2019), doi:10.1021/acsami.9b08189.

30. M. D. Glinchuk, A. N. Morozovska, A. Lukowiak, W. Stręk, M. V. Silibin, D. V. Karpinsky, Y. Kim, S. V. Kalinin, Possible electrochemical origin of ferroelectricity in HfO_2 thin films. *J. Alloys Compd.* (2020), doi:10.1016/j.jallcom.2019.153628.

31. M. Qian, I. Fina, M. C. Sulzbach, F. Sánchez, J. Fontcuberta, Synergetic Electronic and Ionic Contributions to Electroresistance in Ferroelectric Capacitors. *Adv. Electron. Mater.* (2019), doi:10.1002/aelm.201800646.

32. C. Ferreyra, M. Rengifo, M. Sanchez, A. Everhardt, B. Noheda, D. Rubi, On the key role of oxygen vacancies electromigration in the memristive response of ferroelectric devices. To appear in Physical Review Applied, *arXiv:2006.10891 V1* (2020).

33. M. Pešić, F. P. G. Fengler, L. Larcher, A. Padovani, T. Schenk, E. D. Grimley, X. Sang, J. M. LeBeau, S. Slesazeck, U. Schroeder, T. Mikolajick, Physical Mechanisms behind the Field-Cycling Behavior of HfO_2-Based Ferroelectric Capacitors. *Adv. Funct. Mater.* (2016), doi:10.1002/adfm.201600590.

34. P. Gao, C. T. Nelson, J. R. Jokisaari, S. H. Baek, C. W. Bark, Y. Zhang, E. Wang, D. G. Schlom, C. B. Eom, X. Pan, Revealing the role of defects in ferroelectric switching with atomic resolution. *Nat. Commun.* (2011), doi:10.1038/ncomms1600.

35. Materials and Methods are available as Supplementary Materials on Science Online.

36. S. de Graaf, J. Momand, C. Mitterbauer, S. Lazar, B. J. Kooi, Resolving hydrogen atoms at metal-metal hydride interfaces. *Sci. Adv.* (2020), doi:10.1126/sciadv.aay4312.

37. G. Sanchez-Santolino, M. Cabero, M. Varela, J. Garcia-Barriocanal, C. Leon, S. J. Pennycook, J. Santamaria, Oxygen octahedral distortions in LaMO3/SrTiO3 superlattices, *Microscopy and Microanalysis* (2014), doi: 10.1017/S1431927614000750.

38. S. Stølen, E. Bakken, C. E. Mohn, Oxygen-deficient perovskites: Linking structure, energetics and ion transport. *Phys. Chem. Chem. Phys.* (2006), doi:10.1039/b512271f.

39. P. Nukala, M. Ahmadi, J. Antoja-Lleonart, S. de Graaf, Y. Wei, H. W. Zandbergen, B. J. Kooi, B. Noheda, In situ heating studies on temperature-induced phase transitions in epitaxial Hf0.5Zr0.5O2/La0.67Sr0.33MnO3 heterostructures. *Appl. Phys. Lett.* (2021).

40. L. Cao, O. Petracic, P. Zakalek, A. Weber, U. Rücker, J. Schubert, A. Koutsioubas, S. Mattauch, T. Brückel, Reversible Control of Physical Properties via an Oxygen-Vacancy-Driven Topotactic Transition in Epitaxial $La_{0.7}Sr_{0.3}MnO_{3-\delta}$ Thin Films. *Adv. Mater.* (2019), doi:10.1002/adma.201806183.

41. L. Yao, S. Inkinen, S. Van Dijken, Direct observation of oxygen vacancy-driven structural and resistive phase transitions in $La_{2/3}Sr_{1/3}MnO_3$. *Nat. Commun.* (2017), doi:10.1038/ncomms14544.

42. C. Baeumer, C. Schmitz, A. H. H. Ramadan, H. Du, K. Skaja, V. Feyer, P. Muller, B. Arndt, C. L. Jia, J. Mayer, R. A. De Souza, C. Michael Schneider, R. Waser, R. Dittmann, Spectromicroscopic insights for rational design of redox-based memristive devices. *Nat. Commun.* (2015), doi:10.1038/ncomms9610.

43. L. Bégon-Lours, M. Mulder, P. Nukala, S. De Graaf, Y. A. Birkhölzer, B. Kooi, B. Noheda, G. Koster, G. Rijnders, Stabilization of phase-pure rhombohedral $HfZrO_4$ in pulsed laser deposited thin films. *Phys. Rev. Mater.* (2020), doi:10.1103/PhysRevMaterials.4.043401.

44. Y. Wei, S. Matzen, T. Maroutian, G. Agnus, M. Salverda, P. Nukala, Q. Chen, J. Ye, P. Lecoeur, B. Noheda, Magnetic Tunnel Junctions Based on Ferroelectric $Hf_{0.5}Zr_{0.5}O_2$ Tunnel Barriers. *Phys. Rev. Appl.* (2019), doi:10.1103/PhysRevApplied.12.031001.

45. W. Hamouda, C. Lubin, S. Ueda, Y. Yamashita, O. Renault, F. Mehmood, T. Mikolajick, U. Schroeder, R. Negrea, N. Barrett, Interface chemistry of pristine TiN/La: $Hf_{0.5}Zr_{0.5}O_2$

capacitors. *Appl. Phys. Lett.* (2020), doi:10.1063/5.0012595.

46. S. Santucci, S. Sanna, N. Pryds, V. Esposito, ; Energy, J. Byun, T. Min, J. Lee, ; Physics, I. Rungger, E. Plekhanov, D. Banerjee, A. Droghetti, D. Newns, C. Weber, G. J. Martyna, "Defective Metal Oxides-New Generation of Electrostrictor Materials First-Principles Studies of the Effects of Oxygen Vacancies on the HfO2-Based Ferroelectric Tunnel Junction" (2016).

47. A. Herpers, C. Lenser, C. Park, F. Offi, F. Borgatti, G. Panaccione, S. Menzel, R. Waser, R. Dittmann, Spectroscopic proof of the correlation between redox-state and charge-carrier transport at the interface of resistively switching Ti/PCMO devices. *Adv. Mater.* (2014), doi:10.1002/adma.201304054.

48. G. Radaelli, D. Gutiérrez, F. Sánchez, R. Bertacco, M. Stengel, J. Fontcuberta, Large room-temperature electroresistance in dual-modulated ferroelectric tunnel barriers. *Adv. Mater.* (2015), doi:10.1002/adma.201405117.

49. U. Johansson, U. Voigt, A. Mikkelsen, NanoMAX : a hard x-ray beamline at MAX IV, *X-ray nanoimaging: instruments and methods* (2013), doi: 10.1117/12.2026609

50. A. Björling et al., Pytchographic characterization of coherent nanofocussed x-ray beam, Optics Express (2020), doi: 10.1364/OE386068

51. Z. Horita, T. Sano, M. Nemoto, Energydispersive x-ray microanalysis in the analytical electron microscope. *isij Int.* (1989), doi:10.2355/isijinternational.29.179.

52. F. P. G. Fengler, M. Pešić, S. Starschich, T. Schneller, C. Künneth, U. Böttger, H. Mulaosmanovic, T. Schenk, M. H. Park, R. Nigon, P. Muralt, T. Mikolajick, U. Schroeder, Domain Pinning: Comparison of Hafnia and PZT Based Ferroelectrics. *Adv. Electron. Mater.* (2017), doi:10.1002/aelm.201600505.

53. https://dataverse.nl/doi:

Acknowledgments and Funding: PN would like to acknowledge funding from European Union's Horizon 2020 research and innovation programme under Marie Sklodowska-Curie grant agreement #794954 (nickname: FERHAZ). MA, YW, BJK and BN acknowledge the financial support of the CogniGron research center and the Ubbo Emmius Funds (Univ. of Groningen). YW and SM acknowledge a China Scholarship Council grant and a Van Gogh travel grant. We acknowledge MAX IV Laboratory for time on Beamline NanoMAX under Proposal 20190954. Research conducted at MAX IV, a Swedish national user facility, is supported by the Swedish Research council under contract 2018-07152, the Swedish Governmental Agency for Innovation Systems under contract 2018-04969, and Formas under contract 2019-02496. SM acknowledges the French RENATECH network that supported the cleanroom activity.

PN acknowledges all the discussions with Pratyush Buragohain from the University of Nebraska.

The data is available on University of Groningen data repository (*53*)

Author contributions: PN, BN, MA and DC conceived the idea. PN synthesized the samples through PLD. MA, PN devised the in situ biasing device preparation protocol using FIB, and made the devices. PN, MA and SG set-up the electrical biasing system compatible with Themis-Z

microscope. PN, MA and SG carried out the in situ biasing experiments with timely help from HWZ and BJK. YF and SM synthesized and fabricated tunnel junction and capacitor devices and did the ex situ electrical testing. PN, MA prepared the lamellae and carried out imaging experiments. PN, MA, YF, TC and SG analyzed the TEM and transport data. DC, AB and DM carried out the experiments on the beamline. ES, PN, DC and AB carried out synchrotron data analysis. All the authors discussed the data. PN, BN co-wrote the manuscript, which was read, edited and approved by all the authors.

Competing interests: The authors declare no competing interests.

Supplementary Materials:

Materials and Methods

Supplementary text, S1-S10

Fig. S1-S11

Figure captions:

Fig. 1: Deoxygenation of bottom electrode LSMO layer with increasing positive bias. (a) iDPC-STEM image of a representative region of the bottom LSMO layer in the virgin state, viewed along the [110] zone axis, exactly matching the perovskite structure. Schematic in the inset showing MnO_6 octhahedra and their antiphase tilts, clearly imaged in (A). (inset) La/Sr: green, Mn: red, O:brown). (B) iDPC-STEM image at V= 2 V. Panels on the right show various unit cells, illustrating Mn columns (circled in white) and their displacements (marked by green arrows) away from the center of an octahedron. Oxygen columns are marked in red circles. (C) iDPC-STEM at 4 V. BM LSMO (zone axis: *a*, schematic in inset) denoted by alternating MnO_4 tetrahedra and MnO_6 octahedra along *c'*. (D) Schematic showing the evolution of an MnO_6 octahedra in the virgin state (enclosed in black box) towards MnO_5 square pyramids at 2 V (enclosed in red box) to alternating MnO_4 tetrahedra and MnO_6 octahedra at 4 V (enclosed in blue). (E) Plot of variation of *c*' (La-La distance) parameter from the STO interface in perovskite (black), BM-precursor (red) and BM phases (blue). (F) Overview image of LSMO/HZO/LSMO capacitor with regions marked where oxygen content was quantified from EDS (G) at 0 V and 1.5 V. Scale bars, 1 nm in (A-C), and 5 nm in (F).

Fig. 2: Oxygenation of bottom electrode LSMO layer with increasing negative bias. iDPC-STEM images of a region in the same field of view at 0 (A) and -1.3 V (B). At -1.3 V oxygen columns start to appear (marked by red arrows) in positions where there were none in the BM phase at 0 V. (C) BM phase transforms to BM precursor phase at -3 V and is retained so at 0 V (D). (E) Dynamics is recorded via HAADF-STEM imaging within 120 seconds of ramping from 0 to 3 V from a starting perovskite phase. A BM-precursor phase is imaged at 60 sec, BM phase is imaged at 120 sec. (F) Upon changing the bias to -3 V, a BM phase is recorded at 30 sec, changes to perovskite phase by 90 sec (disappearance of the superstructure spots in FFT, Fig. S4). The intermediate BM-precursor phase recorded at 60 sec, converts to perovskite-like phase in about 6 sec as can be seen by the variation in c' parameter, giving an idea about the time scales of $\ddot{V}_o$ migration. Scale bars: 1 nm in (A-D) and 5 nm in (E-F)

Fig. 3: Oxygenation and deoxygenation of HZO and associated phase transitions. (A) Evolution of an r-phase HZO grain while oxygenating under positive bias followed through iDPC-

STEM image, where both cations and oxygen columns are displayed. The image of the virgin state at 0V shows two red arrows pointing to two oxygen columns in the (100) planes neighboring a cationic column. Multislice iDPC-STEM image simulations of the r-phase (*R3m* symmetry) in the inset shows the good match with the observations. (B) Out-of-plane displacement of $\ddot{V}_o$ with external bias, in the marked supercell (red box) with respect to the positions in (A). Negative values indicate displacement towards bottom electrode. $\ddot{V}_o$ shows both in-plane and out-of-plane (towards bottom electrode) components (inset). (C) A new grain nucleates in the same region at 4 V, giving rise to a polycrystalline nature (FFT in inset). (D) Another region in the HZO film back at 0 V showing o-phase and m-phase (with multislice simulations of both in the insets). Also note the change of orientation from [111] to [100]. (e) iDPC-STEM image of domains (mutually rotated by 180^o about [111]) in the r-phase (to be compared with simulation in inset of Fig. 3a, from ref. *(36)*), which is retained when poled at -3 V (imaged at 0 V). Scale bars: 1 nm in (A, C, E) 2 nm in (D). Interfaces between HZO and top and bottom LSMO are marked in orange. In (D) only HZO/bottom electrode interface is shown.

Fig. 4: Cycled tunnel junctions and ferroelectric capacitors. (A) Co/HZO (2 nm)/LSMO tunnel junction in LRS (500 μs, 100s of cycles poled at -6 V). HAADF-STEM image on the left (scale bar: 5 nm), and iDPC-STEM of a selected region in LSMO on the right (scale bar: 1 nm). (B) Ex-situ imaging of tunnel junction in HRS (500 μs, 100s of cycles, poled at 6 V). (right) HAADF-STEM (and corresponding information from EDS) shows CoOx/HZO/LSMO stack (scale bar: 5 nm). (left) iDPC-STEM of a region in LSMO shows BM-precursor phase (scale bar: 1 nm). Selected Mn column displacements towards a square pyramidal geometry are marked by green arrows. (C) Temperature dependent P-V loops obtained from dynamic hysteresis measurements at 1 kHz in LSMO/HZO (7 nm)/LSMO (30 nm) capacitors. Inset shows the corresponding $2P_r$ vs T curve (see also Fig. S8). (D) iDPC-STEM image of LSMO close to HZO interface (marked in orange) in TiN/HZO (7 nm)/LSMO capacitors, prepared in "down polarized" state (at 5.5 V). BM-precursor phase is formed, confirmed by disorder in *c*' parameter (inset). (E) iDPC-STEM image of a "down" polarized HZO layer, which is structurally still in r-phase (inset left, HAADF-STEM image with the IDPC-STEM image presented for the region in the blue box; inset right, multislice simulation of *R3m* phase). Scale bar in (D) and (E): 1 nm. (F) Schematic of the polarity dependent oxygen voltammetry process in the Metal-Insulator-Metal device structure. Oxygen deficient phases in various layers are represented with lighter colors.

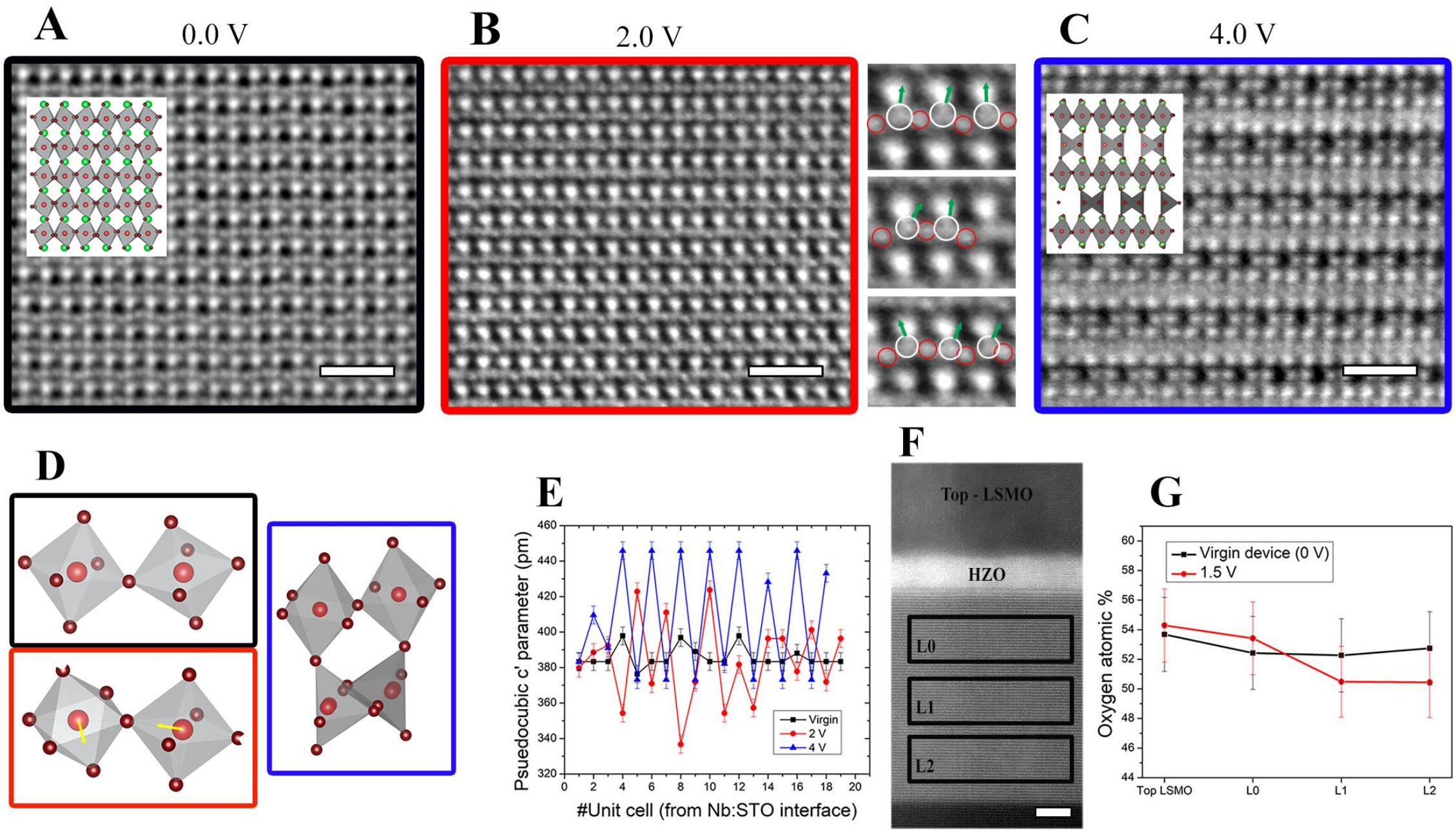
A
0.0 V
B
2.0 V
C
4.0 V
D
E
Psuedocubic c' parameter (pm)
#Unit cell (from Nb:STO interface)
Virgin
2 V
4 V
F
Top - LSMO
HZO
L0
L1
L2
G
Oxygen atomic %
Virgin device (0 V)
1.5 V
Top LSMO
L0
L1
L2

Figure 1

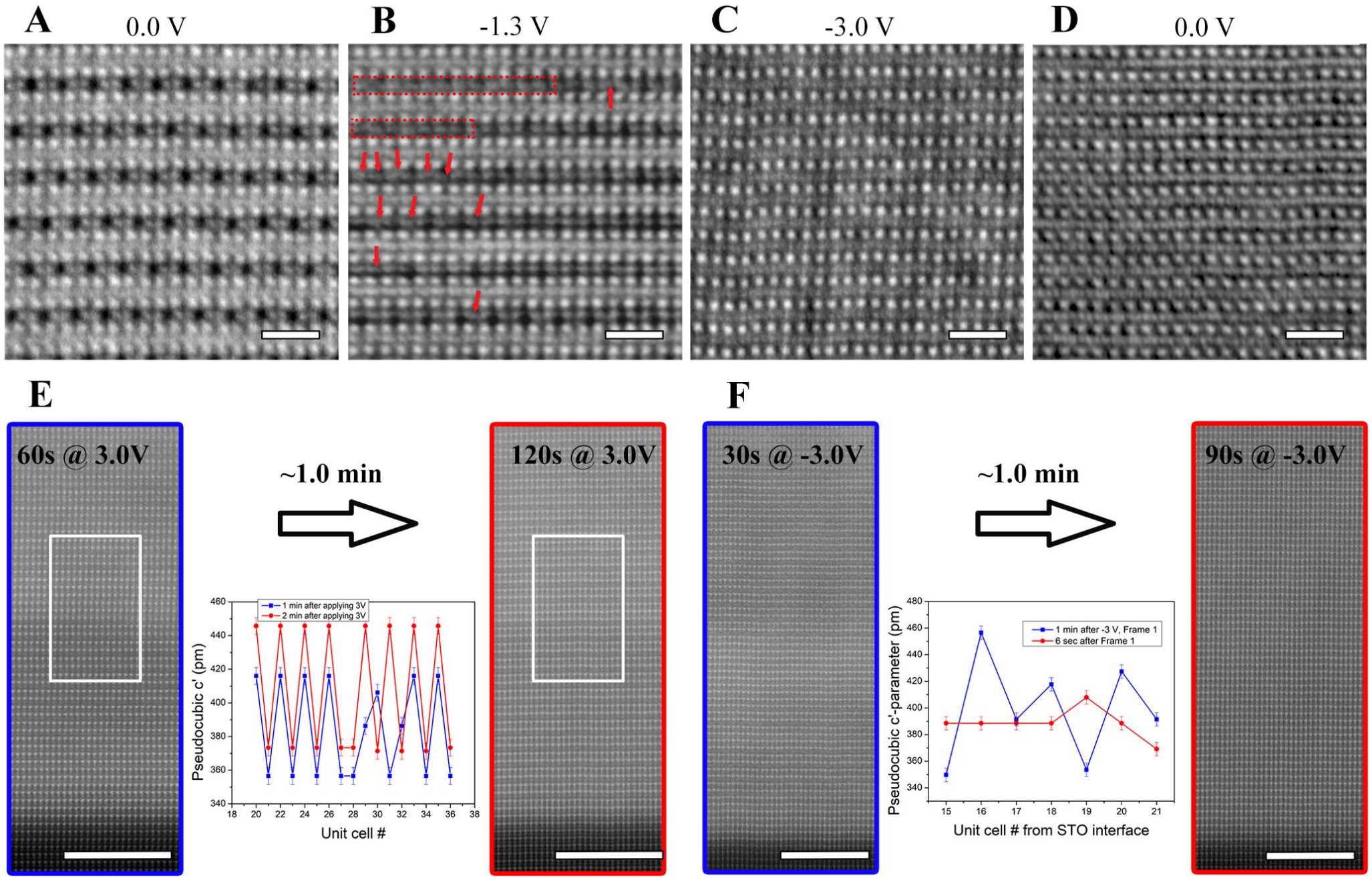
A
0.0 V
B
-1.3 V
C
-3.0 V
D
0.0 V
E
60s @ 3.0V
~1.0 min
120s @ 3.0V
1 min after applying 3V
2 min after applying 3V
Pseudocubic c' (pm)
Unit cell #
F
30s @ -3.0V
~1.0 min
90s @ -3.0V
1 min after -3 V, Frame 1
6 sec after Frame 1
Pseudocubic c'-parameter (pm)
Unit cell # from STO interface

Figure 2

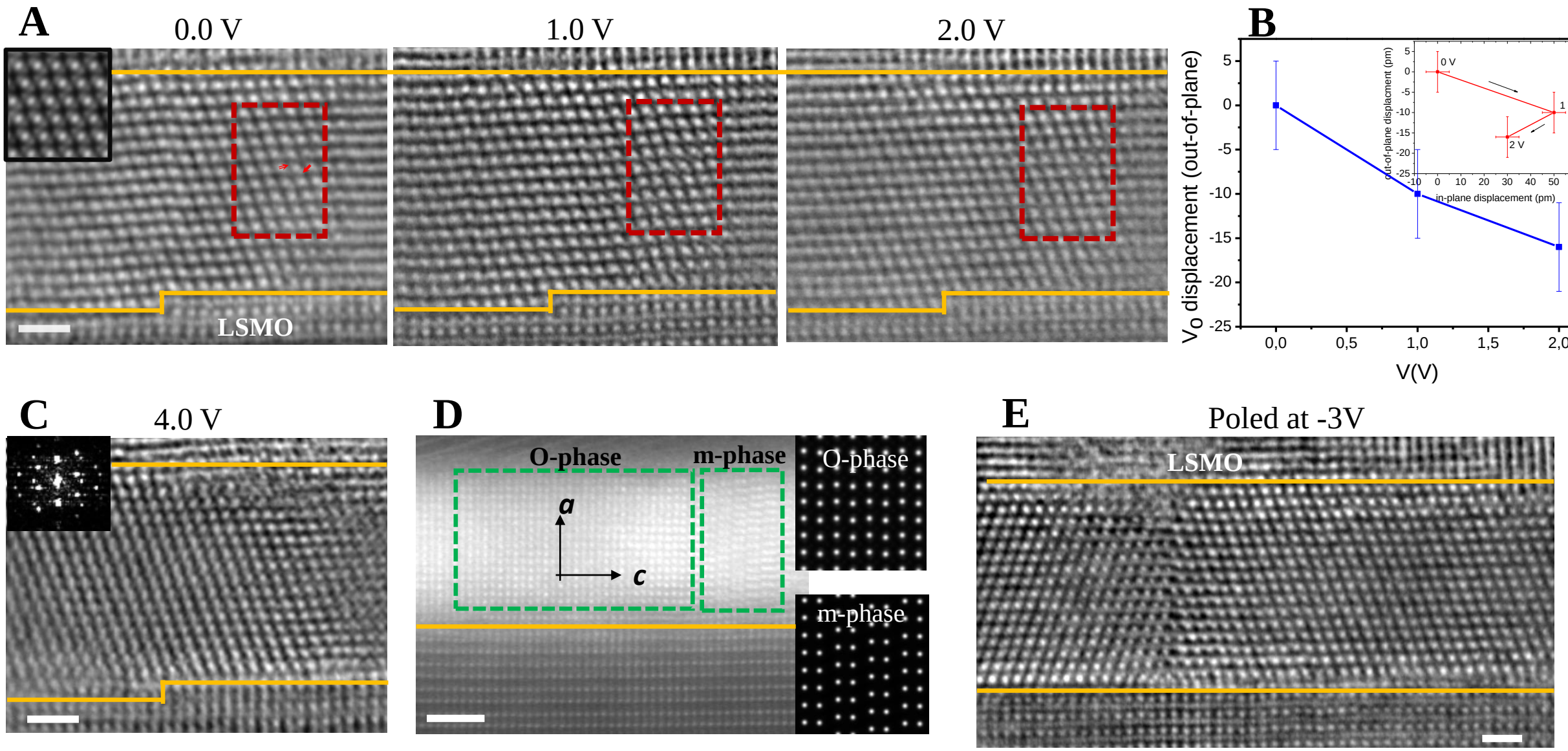
A
0.0 V
1.0 V
2.0 V
LSMO
B
V_O displacement (out-of-plane)
V(V)
0,0
0,5
1,0
1,5
2,0
5
0
-5
-10
-15
-20
-25
0 V
1
2 V
out-of-plane displacment (pm)
in-plane displacement (pm)
C
4.0 V
D
O-phase
m-phase
a
c
O-phase
m-phase
E
Poled at -3V
LSMO

Figure 3

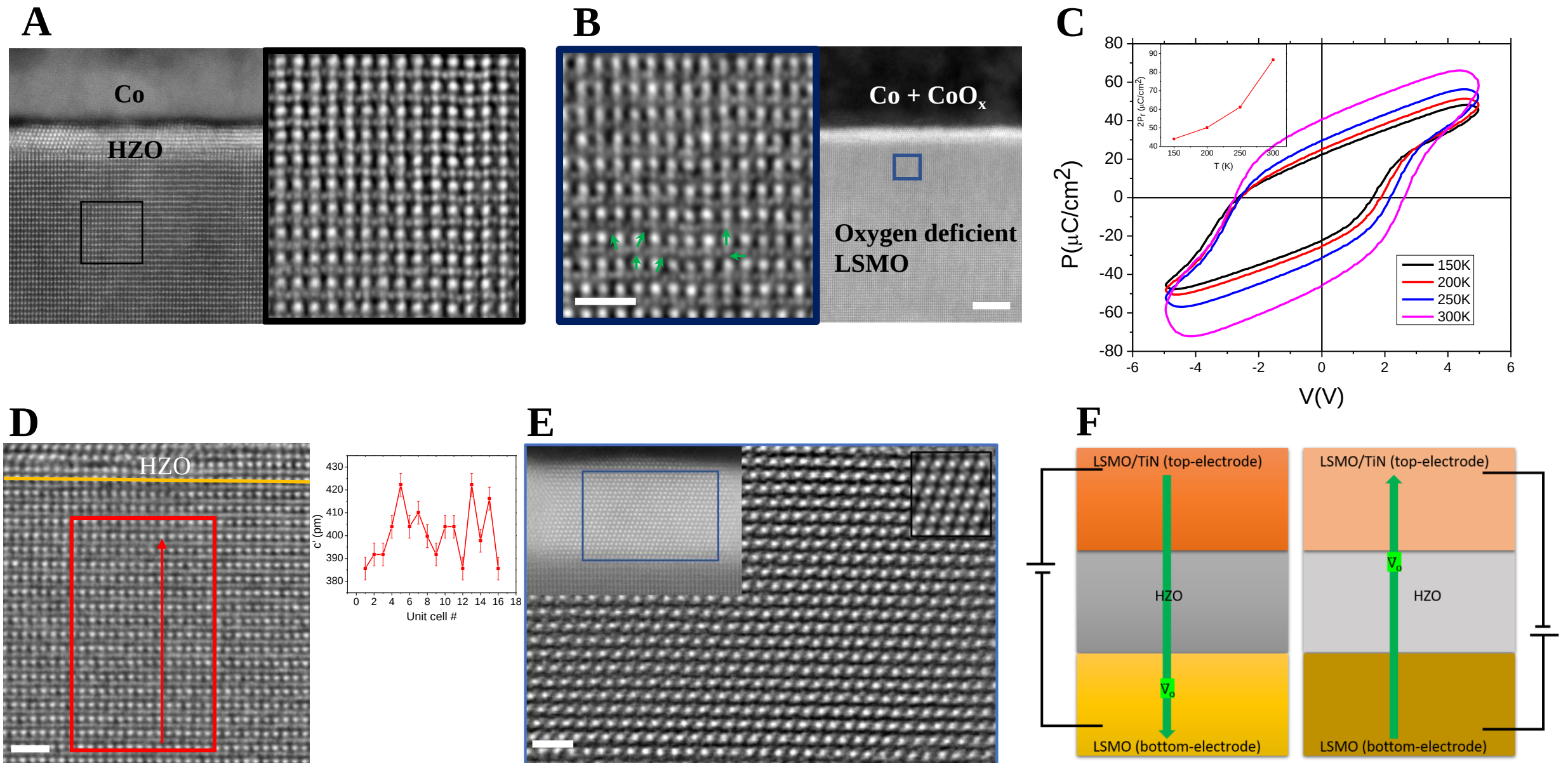
A
Co
HZO
B
Co + CoOx
Oxygen deficient
LSMO
C
P(μC/cm2)
V(V)
150K
200K
250K
300K
2Pr (μC/cm2)
T (K)
D
HZO
c' (pm)
Unit cell #
E
F
LSMO/TiN (top-electrode)
LSMO/TiN (top-electrode)
HZO
HZO
Vo
Vo
LSMO (bottom-electrode)
LSMO (bottom-electrode)

Figure 4

Science
AAAS

Supplementary Materials for

Reversible oxygen migration and phase transition in hafnia-based ferroelectric devices

Authors: Pavan Nukala[1,2*], Majid Ahmadi[1,3], Yingfen Wei[1,3], Sytze de Graaf[1], Evgenios Stylianidis[1,4], Tuhin Chakrabortty[2], Sylvia Matzen[5], Henny W. Zandbergen[6], Alexander Björling[7], Dan Mannix[8-10], Dina Carbone[7], Bart Kooi[1,3], Beatriz Noheda[1,3*]

Affiliations:

[1]Zernike Institute of Advanced Materials, University of Groningen, Groningen, 9747 AG, The Netherlands,

[2]Center for Nanoscience and Engineering, Indian Institute of Science, Bengaluru, 560012, India

[3]CogniGron (Groningen Cognitive Systems and Materials Center), University of Groningen, Nijenborgh NL-9747 AG Groningen, Netherlands.

[4]Department of Physics and Astronomy, University College London, Gower Street, London, WC1E 6BT, United Kingdom

[5]Center for Nanoscience and Nanotechnology, Paris-Saclay University, CNRS, 91120, Palaiseau, France

[6]Kavli Institute of Nanoscience, Faculty of Applied Sciences, Delft University of Technology, 2628 CJDelft, The Netherlands

[7] MAX IV Laboratory, Lund University, 22100 Lund, Sweden

[8] University Grenoble Alpes, CNRS, Institut Néel, 38042 Grenoble, France

[9]European Spallation Source, SE-221 00 Lund, Sweden.

[10]Aarhus University, Langelandsgade 140, DK-8000 Aarhus, Denmark.

*Correspondence to: pnukala@iisc.ac.in, b.noheda@rug.nl

This PDF file includes:

Materials and Methods
Supplementary Text, S1-S10
Figs. S1 to S11

Materials and Methods

Synthesis by Pulsed Laser Deposition: LSMO (30 nm)/HZO (6 nm)/LSMO (30 nm) layers were grown epitaxially on Nb:STO via pulsed laser deposition (PLD). The growth conditions are described elsewhere (*7*). Pt (200 nm) was sputtered on the top-electrode (LSMO).

***In situ* STEM set-up, imaging and biasing techniques:** The set-up of the holder, biasing system in Thermo Fisher Scientific Themis Z (monochromated and double corrected) microscope is shown in Fig. S1A. In-situ biasing cum heating customized double tilt holder (HennyZ, Fig. S1B) was used to host the cross-sectional devices (zone axis: [110] Nb:STO) prepared on a MEMS based SiN_x chip (Fig. S1C,D preparation procedure described in the next section). Biasing was performed through Keithley 4200 parameter analyzer by using two SMUs (source measuring units, Fig S1A). Atomic resolution imaging (while biasing) was performed at 300 kV through HAADF-STEM, and more importantly integrated differential phase contrast (iDPC) STEM to image low Z elements such as oxygen. Beam convergence angle was 22.4 m rad. Data from segmented detectors were acquired under the collection angles from 6-23 mrad. H(M)AADF-STEM images were simultaneously acquired with collection angles > 23 mrad. Energy dispersive spectroscopy (EDS) was performed using two large area detectors in total capturing 1.76 steradian. Spectra were acquired from various regions in the capacitor structure at a combined signal of 10-15 kcps for over 1 hour. Voltage is always applied to the top electrode, with bottom electrode at 0 V (Fig S1E).

***In situ* biasing device fabrication:** MEMS based micro heater & electrical biasing chip (developed by HennyZ, see Fig. S1C-E) is used for hosting the TEM cross-sectional lamella, and connecting the lamella to the external pads. This chip has 6 electrodes, 3 on each side of the SiN_x membrane. The outermost electrodes are connected to the microheater and can heat the TEM lamella very locally up to 1000 ^{o}C. The innermost Pt-electrodes are used for biasing. A focused ion beam (FIB, FEI Helios G4 CX) based sample preparation protocol was developed in-house for *in situ* biasing experiments. Electron transparent regions were created in the region between the inner most electrodes of interest on the SiN_x membrane by drilling a hole using the Ga ion beam. Cross-sectional chunks (dimensions: 10 x 1.5 x 5 μm^3) were initially thinned down to 300-500 nm thickness using standard focus ion beam (FIB) based processing at 30 kV, and then transferred onto the SiN_x membrane of the chip (Fig. S1E). The top (Pt) and bottom electrode (substrate) were then connected to the electrodes on the chip through e-beam induced Pt deposition (EBID). Certain windows (~1 x 3 μm^2) on the lamella were thinned down to ~50 nm using the Ga ion beam at 16

kV accelerating voltage, and finally several low kV cleaning steps (5 and 2 kV) were used not only to clean the side surfaces of the lamella, but also to remove the excess Pt deposition (Fig S1E). Electrical measurements were performed *ex situ* after every step to understand any possible leakage sources, and further milling and cleaning steps were performed to remove these sources.

Regular device fabrication: Tunnel junction devices (Co/HZO (2 nm)/LSMO) were fabricated using the procedure described in ref. *44*. Two types of ferroelectric capacitors were fabricated: TiN/HZO (7 nm)/LSMO (30 nm)//STO devices were made by depositing TiN as the top electrodes using standard photolithography and sputter deposition followed by lift-off procedure on the rest of the stack grown by PLD. LSMO/HZO/LSMO capacitors were also fabricated. The entire stack was first grown using PLD. Then devices were lithographically defined by etching the top LSMO, HZO and 6 nm of bottom LSMO layer away from the regions of interest using Ar ion-beam etching. Cross sections from these devices were made through standard FIB based TEM cross-sectional lamella preparation procedure.

The tunnel junction devices were tested *ex situ* with +6/-6 V sub-millisecond rectangular pulses for 100s of cycles. Cross-section TEM lamellae were made from one sample in the high resistance state, and another one in the low resistance state. The TiN/HZO/LSMO capacitors were tested for ferroelectric switching using the PUND scheme at +/- 5.5 V using triangular pulses of rise and fall time of 250 μs for tens of cycles. Results presented in Fig. 4C-E are from a cross-sectional lamella of such capacitor, which was eventually ferroelectrically switched “down” with a +5.5 V pulse (Fig. S8).

Operando x-ray diffraction:

Au/HZO (6 nm)/LSMO and LSMO/HZO (6 nm)/LSMO capacitors were fabricated using a lithography based process (Fig S9), and tested using *operando* synchrotron X-Ray diffraction at the NanoMAX beam line of the MAX IV synchrotron *(49,50)*, using a nanobeam with 400 nm x 100 nm footprint. Both devices were cycled at 100 Hz in a modest voltage range between -3.5 and 3.5 V for tens of thousands of cycles (Fig S10). The HZO (111) Bragg peak was measured with a 2D pixel detector before and after electrical cycling to observe the impact of the voltage change onto the crystal structure of the device.

Energy dispersive spectroscopy quantification:

EDS spectra of LSMO recorded with the Themis Z electron microscope were quantified after background subtraction using the Brown-Powell model *(51)*. Oxygen atomic percentages in Fig.

1G were determined from 20 x 5 nm^2 regions with one on the top electrode, and three in the bottom electrode with varying distance to the HZO as marked L0, L1 and L2 in Fig. 1F.

$\ddot{V}_o$ displacement analysis in HZO layer:

The cationic lattice of the supercell was first constructed by identifying the cation positions through a peak finding algorithm after assigning a finite width defined by a mask around each peak. The rest of the lattice in the supercell is the anionic lattice (see Fig. S4). We quantify the $\ddot{V}_o$ migration as a function of bias in this supercell by estimating the difference between the centers of mass (CoM) of the cations and anions. Under the assumption that cations do not move at small voltages, we can relate this quantity directly to the migration of $\ddot{V}_o$. The choice of the mask defining the size of the cations, and the pixel size determine the errors in estimation of the displacement, although peak fitting can occur with sub-pixel size precision.

P-V hysteresis measurements:

P-V loops were measured using a dynamic hysteresis measurement scheme on TiN/HZO/LSMO//STO capacitors. A triangular voltage waveform of 1 kHz from 0 to 5 to -5 to 0 V (defining one period) were applied to the device at various temperatures, and corresponding currents were measured. Polarization was calculated using the formula $P = \frac{1}{A}\int i\,dt$, where A is the device cross-sectional area, i is the measured current, and t is the time.

Supplementary Text

S1. The LSMO layer in the as-deposited film is oriented with $[001]_{pseudocubic}$ (c-axis) out of plane, and observed along the $[110]_{pseudocubic\ (pc)}$ (zone axis). Schematics of A-site (La/Sr), B-site (Mn) and oxygen column arrangements are shown in Fig. 1A. The $a^-a^-a^-$ octahedral tilts typical of rhombohedral LSMO reveal themselves as antiphase δ tilts in this zone (alternating positive and negative Mn-O-Mn bond angles)(*35*). Deviations of Mn columns from octahedral coordination in the virgin state, although present are very minimal, and can be considered to be disorder induced perturbations of the standard structure. Even some disorder in the octahedral tilt angles (165-176^o) can be seen in Figs 1A and S2A.

S2: Square pyramidal coordination is typical of the BM phases of strontium manganite (SMO, $SrMnO_{2.5}$, Fig. S2D). When BM-SMO is viewed along $[110]_{pc}$ zone axis, it shows two important features (i) Mn displacements away from the octahedral coordination along $[1\text{-}10]_{pc}$ and (ii) a resolvable doubling of alternate oxygen columns between Mn columns with ~90 pm projected

distance between the columns along $[1\text{-}10]_{pc}$ (horizontal direction in Fig.1B, Fig. S2B,D). Both these features, characteristic of square pyramidal coordination are present in the BM precursor phase of LSMO (Fig S2C, Mn displacement marked in green arrows, Oxygen column separation marked by blue arrows), albeit in randomly varying directions (not just along [1-10]). The reported changes in structure at 2 V (Fig. 1B) are hysteretic and remain upon removing the external bias.

In the following we present the Mn displacements and corresponding histograms for both the device in virgin state, as well as several regions for the device biased at 2V. Mn positions and O positions were computed as the centroid of the Mn and O atomic column intensity distributions, respectively. Displacement of Mn from the center of the oxygen octahedron was calculated as the difference between the position of Mn and the center of mass of O-O bond on either side of the Mn. Angle of the displacement is measured with respect to the in-plane direction (horizontal). Arrow plots are shown in Fig. S3A,B, to visualize the displacements directly on the images.

Fig. S3A shows the displacement vectors of a representative region in the virgin state, where we measured no significant Mn displacement (<5 pm, which is within the sensitivity of the measurement). This is consistent with our diagnosis of virgin state as consisting mostly of regular MnO_6 octahedra (non-distorted).

Fig. S3B shows two representative regions biased at 2 V. Here, we indeed see random displacements of Mn atoms (with displacement magnitudes as large as 50 pm). These analyses were carried out on 6 different regions of interest across various images. The polar scatter plot of Mn displacements (on circles of radius 60 pm) comparing the virgin state (from 60 Mn columns) and the biased state (from 329 Mn columns) is shown in Fig. S3C. While in virgin state there are almost no displacements, in the biased state the displacements vary from 0 to 55 pm (mean value :18.6 pm, std. deviation:10.2 pm) with random angular dispersion. These displacements result in a distortion of an octahedron into square pyramids, a prominent feature of the BM-precursor phase, further validating our previous claims on the structure of this phase.

S3: In the BM phase shown in Fig. 1C (viewed along a-axis), the perovskite-like layer consists of MnO_6 octahedra, whereas the oxygen deficient Mn-O layer consists of MnO_4 tetrahedra, which along the [1-10] direction, alternate between pointing towards each other and away from each other. Also observable is another domain viewed along c-axis (Fig. S3A), where Mn columns in the oxygen deficient Mn-O layer appear more symmetrically arranged. In Fig. S3B, a region is shown with the field of view of both the BM domains.

S4: Oxygen vacancies are known to cause some lattice expansion even in virgin samples. These vacancies are typically a result of not just the growth conditions of the film, but also the fact that LSMO grows under tensile strain on STO and Nb:STO (which promotes oxygen vacancies). See ref (*6*).

S5: We classify the effects that we observe in various experiements as short-term and accumulated short-term and long-term effects. For clarity we define our various experiments as follows:

a) Short term effects: (a) 100-few kHz switching, <10 cycles, <6 V (Fig 4D,E) ; (b) 100-few kHz switching, tens of thousands of cycles at <3.5 V (operando synchrotron cycling experiments)
b) Accumulated short term effects: 100-few kHz switching, hundreds of cycles @ 6 V (tunnel junctions, Fig 4A,B, Fig. S7)
c) Long term effects: DC stressing (in-situ TEM experiments, and operando XRD DC biasing experiements)

It may be seen that voltage time dilemma is taken into consideration in definining these effects. For e.g. hundreds of cycles @ 6V still shows a more accumulated short-term effect, than tens of thousands of cycles @ 3.5 V.

S6: The saturation polarization (P_s) of the unit cell (as shown in Fig. S5C) is estimated in 2 different ways.

(i) Through a peak-fitting algorithm the anionic positions (y_i) and cationic positions (x_i) were obtained in a unit cell. Then $P_r=\Sigma(4x_i-2y_i)/V$, where V is the Volume of the unit cell (4 and -2 are the Born effective charges of Hf/Zr and oxygen respectively). The unit cell was chosen such that $P_r = 0$ in the symmetrized paraelectric phase (ref. *7*). This yielded $P_r< 2$ μC/cm^2 (displacement < 10 pm) for HZO across 14 different unit cells in the *R3m* phase. This procedure assumes HZO is completely stoichiometric, and P_r was similarly estimated on the *R3* phase in ref *40*. Note that for similar samples in *R3m* phase, P_r=35 μC/cm^2 was measured through macroscopic electrical switching experiments.

(ii) With the new information from this work on the oxygen deficiency of the *R3m* HZO phase, the stoichiometric assumption presented in (i) does not hold. So, we calculated the P_r by estimating the center of mass of the cationic lattice and the non-cationic part (anionic lattice) in every unit cell (Fig. S5C). The difference in the center of masses

gives a displacement of ~38 (±8) pm in the unit cell shown in Fig. S5C (from the domain on the left in Fig. 3E in the manuscript). This suggests that $\ddot{V}_o$ is responsible for almost 4 times increase in the displacement (compared to the stoichiometric lattice in (i)). Whether this will cause significant improvement in direct estimation of P_r cannot be established without the knowledge on the Born charges of cations and anions in this oxygen deficient HZO lattice. Upon assuming that the cationic born charges in this configuration still remains +4, we estimate $P_r < 9$ μC/cm^2. In any case, there exists a clear mismatch with the value obtained from electrical measurements, strongly supporting that most of the switching arises from oxygen voltammetry process.

S7: The increase of remnant polarization (P_r) with temperature presented in Fig. 4C (see also Fig. S6) is consistent with the fact that $\ddot{V}_o$ migration kinetics improves with temperature, clarifying that polarization switching and $\ddot{V}_o$ are intertwined mechanisms. In conventional ferroelectrics, P_r is expected to degrade with increasing temperature owing to increased thermal fluctuations. Note that similar unconventional behavior was measured by Fengler and coworkers from 25^{o}C to 125^{o}C on ALD deposited HZO samples with TiN electrodes in ref *52*.

Another interesting observation from these measurements is the pronounced presence of imprint (internal field) at low temperatures, which decreases towards zero at room temperature. This can be rationalized as a result of increased sluggishness of the oxygen diffusion during the topotactic phase transitions that follow oxygen migration (discharge mechanism) at low temperatures, resulting in accumulation of charged vacancies and thus space charge (*32*). However, detailed modeling of this interesting aspect belongs to the gamut of further work.

S8: To address the question of what will happen if one of the electrodes cannot be a sink or source of oxygen, we present results of *operando* X-ray diffraction measurements from Au/HZO/LSMO devices and compare them with LSMO/HZO/LSMO devices. Upon cycling, Au/HZO/LSMO capacitors show FE switching peak on the positive bias side, and different leakage/field-assisted tunneling characteristics for the up and down polarized state on the negative bias side (Fig. S10A). We have measured the (111) Bragg peak of HZO with a 2D detector in a fixed position (Fig. S10B) before, during and after cycling. This peak contains a bright specular part (with specular contributions from all the interfaces of the heterostructure in addition to the Bragg peak of HZO),

and a diffuse off-specular part (only arising from HZO). By masking the specular part, and projecting and interpolating the detector image onto the 2θ axis (2θ projection), we can analyse the changes in the (111) lattice parameter of HZO upon biasing. The cycling was performed at 100 Hz between -3.5 and 3.5 V (Fig. S10C) for tens of thousands of times. Note that this is a modest cycling at low voltages and effects of fatigue need not to be considered. Thus this is still short-term ferroelectricity, as defined in *S5*.

Measurements on the virgin samples in both types of capacitors are consistent with the growth of rombohedral HZO along the [111] direction , with a Bragg peak position at $2\theta=26.5^{o}$ or $d_{(111)}=2.98$ A^{o} (Fig. S10D,E). For the LSMO/HZO/LSMO devices, diffraction measurements of the cycled state do not show any signficant difference (Fig. S10D). However, in the case of Au/HZO/LSMO, we see that a peak appears at $2\theta=24.9^{o}$ upon cycling, consistent with the presence of the monoclinic phase of HZO, that coexists with the r-phase (Fig. S10E,F). This confirms that the HZO layer itself is forced to act as source/sink of oxygen vacancies when Au is used as a top electrode, resulting in a reversible phase transitions even with low voltage pulses and modest cycling. In other words, even for short term ferroelectric switching, the HZO layer in Au/HZO/LSMO devices acts as a sink and a source of oxygen vacancies (and not just a conduit), and this results in phase transitions even in HZO.

Finally, we also followed the changes in the lattice parameters of HZO by applying DC bias from 0 to 3.5 V after cycling. We observe that the contribution from the monoclinic phase increases steadily with increasing positive bias (Fig. S11), which is the same long term effect seen in the LSMO/HZO/LSMO capacitors using in situ TEM measurements.

S9: Our thesis is that oxygen vacancy migration is very much intertwined with polarization switching, and that these are not independent from each other. It has been repeatedly reported that in hafnia-based ferroelectrics (unlike in conventional ferroelectrics), P_r increases as the film thickness decreases. This is very much consistent with our thesis. We remain agnostic about how exactly the oxygen migration couples to polarization switching and deem this to be a problem for the future.

S10: Another implication of the present work is the estimation of the field drop across the insulator in Metal-Insulator-Metal stacks. With an oxygen conducting memristor such as LSMO as one of

the metals, (e.g. Metal-HZO-LSMO) stacks, field drops (in context of coercive field estimations) across the insulator are typically overestimated due to not considering the field drop in the LSMO layer when oxygen begins to migrate. Thus, in this work we do not mention the fields, rather just report the values of voltages during electrical biasing.

Supplementary Figures

Fig. S1

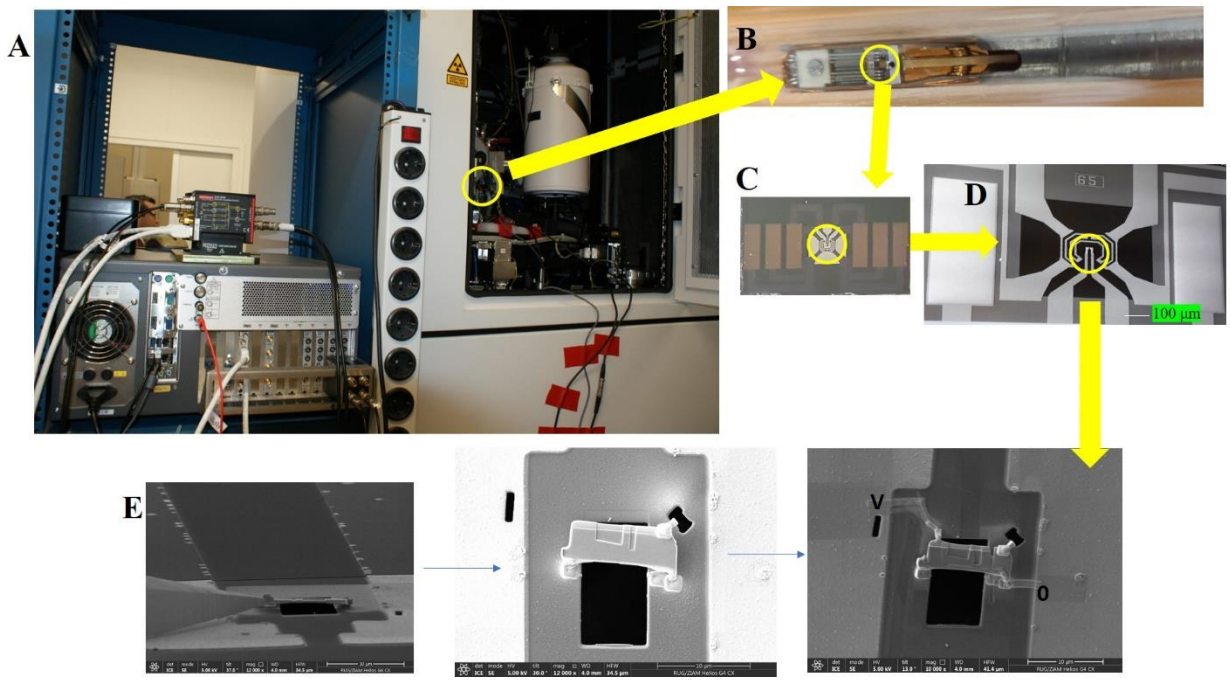

In-situ biasing set-up and sample preparation

(A) Set-up showing Keithley 4200 parameter analyzer with two SMUs connected through a switch box (PMU) to the two leads of an in-situ biasing holder, inserted inside the electron beam column. (B) Optical photo of the biasing/heating holder with the inner two leads for biasing, and outer four to resistively heat the MEMS chip, shown in (C). (D) SEM image of the SiN_x (300 nm) membrane hosting the micro-heater, as well as biasing electrodes (inner most). (E) FIB based lamella transfer procedure onto the SiN_x membrane with electron transparent hole created *a-priori* (protocol described in materials and methods).

Fig. S2

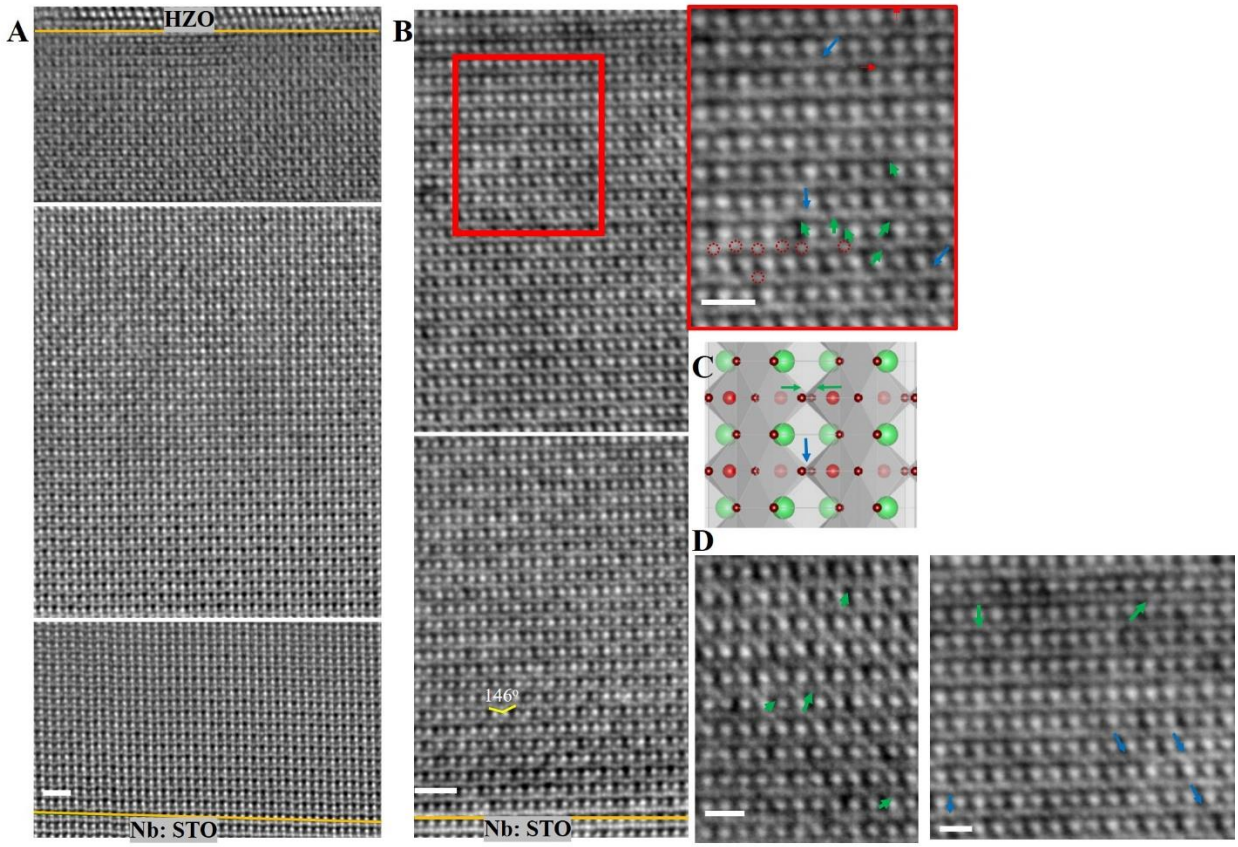

Understanding the structural features of perovskite and BM-precursor phases

(A) Overview iDPC-STEM stitched images in the virgin state. (B) Overview iDPC-STEM stitched images at 2 V. Region enclosed in the red box is zoomed in the inset. Exaggerated octahedral tilts (143-146^{o}) can be seen close to the interface with Nb:STO. In the inset of b, apart from marking selected oxygen column positions (red dotted circles), and Mn displacements from the center of an octahedron (green arrows), we also point out to some of the resolvable double oxygen columns between Mn columns (blue arrows). This is another feature of transformation towards square pyramidal coordination of Mn, as illustrated from the schematic of BM $SrMnO_{2.5}$ (SMO) in (C). (D) iDPC-STEM images from other regions (also in BM-precursor phase), where also Mn displacements (green arrows), and resolvable separation between oxygen columns between Mn columns (blue arrows) are marked. Scale bars, 1 nm in (A,B), 500 pm in (D) and inset (right panel) of B.

Fig. S3

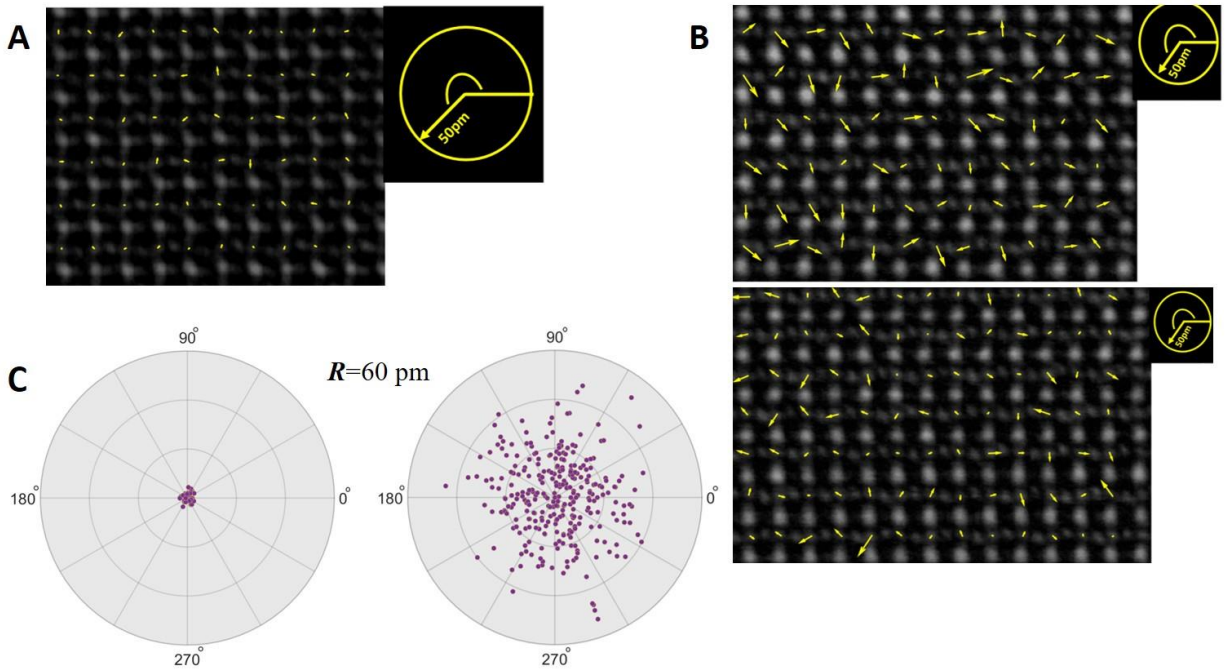

Statistical characterization of Mn displacements in BM precursor phase and virgin state (A) IDPC-STEM image of the LSMO layer in an LSMO/HZO/LSMO/Nb:STO device prior to the application of a bias voltage, with Mn displacements away from the center of the octahedron marked as arrows. (B) IDPC-STEM images of two representative regions in the LSMO layer of the same device with the Mn displacements away from the center of the octahedron marked as arrows. Note the larger random displacements compared to (A). (C) Polar scatter plot of Mn displacement vectors on a 60 pm radius circle for the virgin state (left, obtained from 60 Mn atomic columns) and the 2V biased state (right, obtained from 329 Mn atomic columns).

Fig. S4

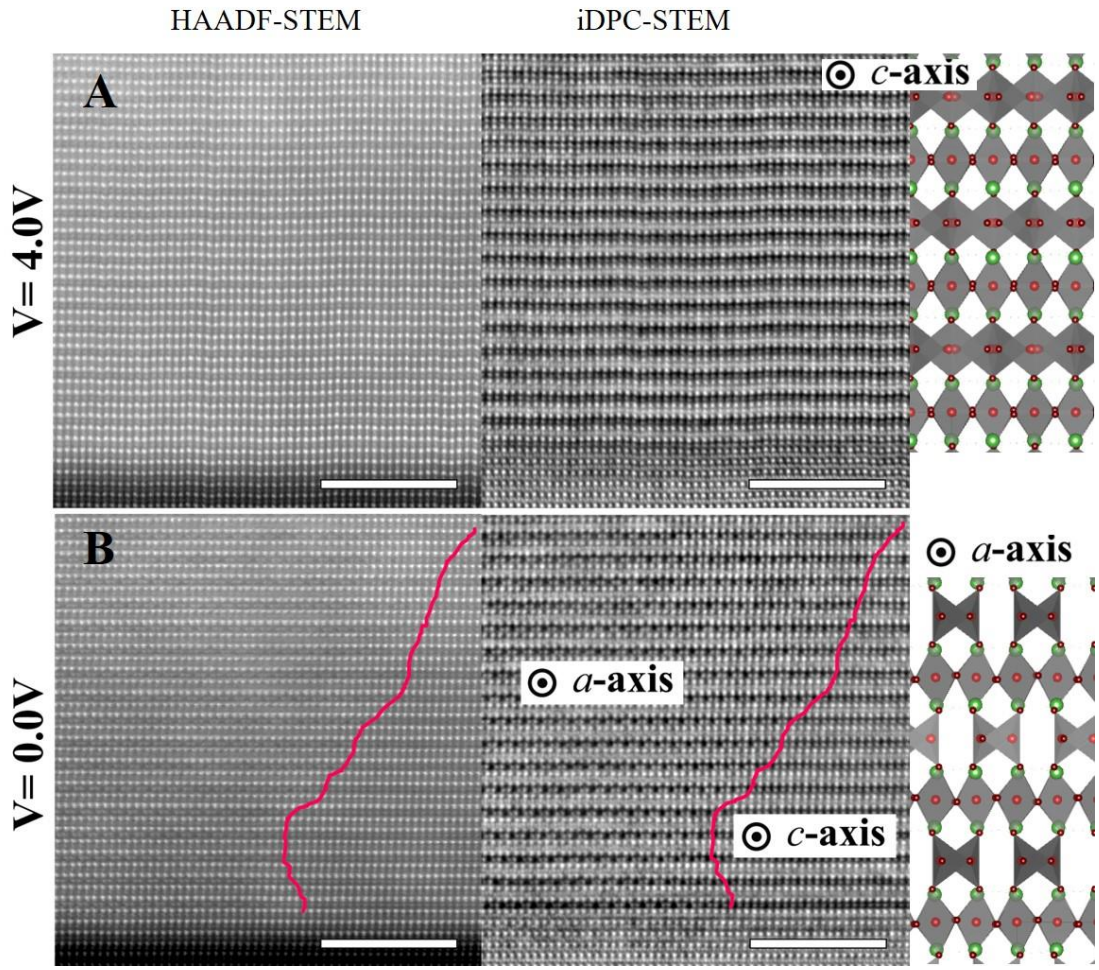

Hysteretic BM phase: (A) HAADF-STEM and corresponding iDPC-STEM images of BM phase formed at 4 V. This is a domain whose c-axis is parallel to the viewing direction (zone axis). Schematic of this domain is also shown on the right most panel (La/Sr: green, Mn: red, O: brown). By comparing HAADF and iDPC-STEM images, it can be clearly noted that the first 2-3 monolayers of LSMO near the interface with the substrate are still in a BM-precursor phase. (B) HAADF-STEM and corresponding iDPC-STEM images of BM phase hysterically retained at 0 V. In the field of view, two domains of the BM phase can be noted (beyond the first 3 monolayers of LSMO near the substrate). They have *a* and *c* as the zone axes respectively. The back-to-back tetrahedra in alternate Mn-O planes along [1-10] direction can be clearly observed from the domain viewed along a-axis (schematic in the right panel).

Fig S5

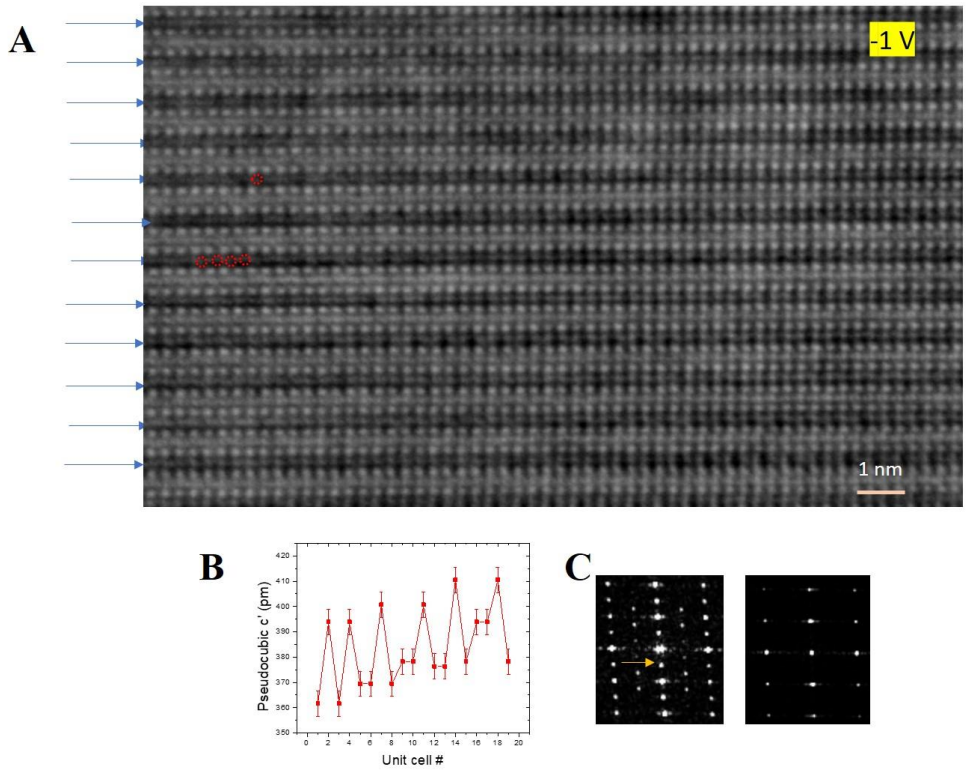

Reoxygenation of LSMO at negative bias and dynamics

(A)This iDPC-STEM image is obtained from a representative region in LSMO which has initially transformed to a BM phase upon poling at 4 V. Then, by applying -1 V, we clearly see oxygen columns appearing (some of them marked by red circles as a guide to eye) in the Mn-O planes in darker contrast (marked by blue arrows on the left). The appearance of these new positions also marks a transformation of this Mn-O layer with Mn in tetrahedral coordination to a Mn in higher coordination. (B) *c*' parameter oscillation across 20 unit cells of LSMO corresponding to Fig. 2C (poled at -3 V), reminiscent of the BM precursor phase. (C) Evolution of BM phase to perovskite phase within 90 seconds of changing the voltage from -3 V to +3 V, followed through Fast Fourier Transforms (for images presented in Fig. 2E). Notice the disappearance of the superstructure reflections upon this transformation.

Fig. S6

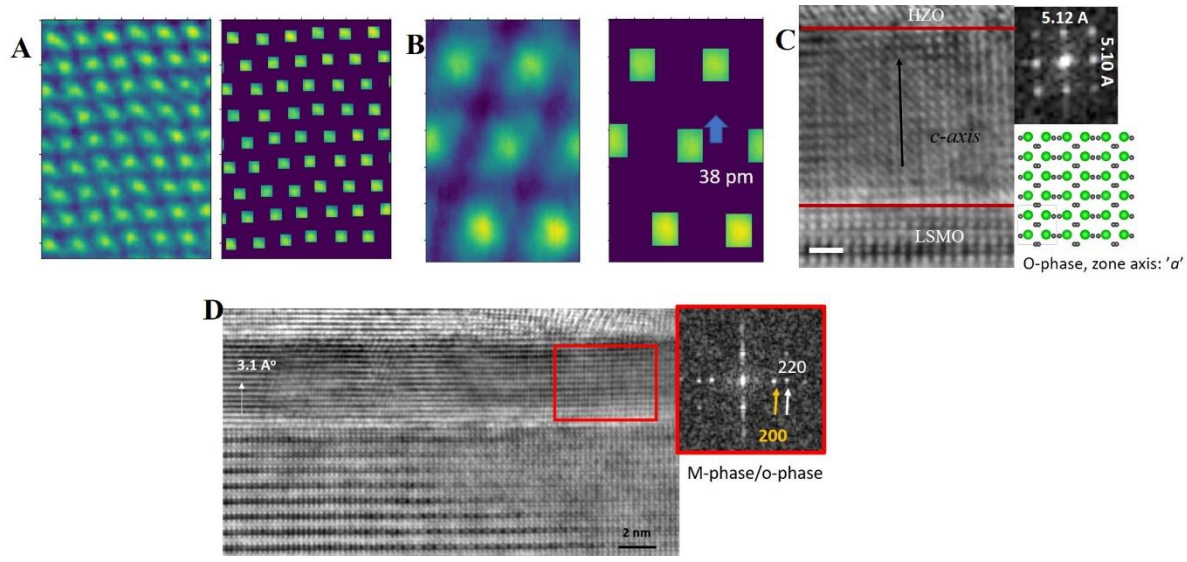

Evolution of HZO layer

(A)The iDPC-STEM image of supercell of HZO r-phase grain presented in Fig. 3A at 1 V (left). Cationic lattice is shown on the right. The rest (difference image) is the anionic lattice. Difference in the CoM of cationic and anionic lattice reveals the $\ddot{V}_o$ displacement as a function of bias (Fig. 3B). (B) *R3m* unit cell (iDPC-STEM image of the left domain in Fig. 3E) considered for direct P_r estimations. Upon symmetrizing this unit cell, P_r=0 in the paraelectric phase, and this justifies the selection of the unit cell. CoM cation−CoM non cationic part gives the displacement (38 pm in the unit cell shown here). This procedure includes the presence of $\ddot{V}_o$, information present in the raw image contrast. (C) iDPC-STEM image of an o-phase with c-axis out-of-plane, observed at 4 V. FFT and the matching of experimental image to the real space schematic with Hf/Zr columns in green, and oxygen in grey confirm an o-phase. (D) Representative large field of view image of the LSMO/HZO/LSMO capacitor imaged after switching twice (switching cycle ends in 3V). Multigrained nature of HZO (either in m or o-phases) can be easily identified from FFT of the indicated region on the right side of the image. In the grain on the left side of the image, the c-parameter (3.1 A^o) corresponds to the m-phase. Thus the r to o/m phase transition (and single grain to multigrainedness) is a reversible process in these experiments.

Fig. S7

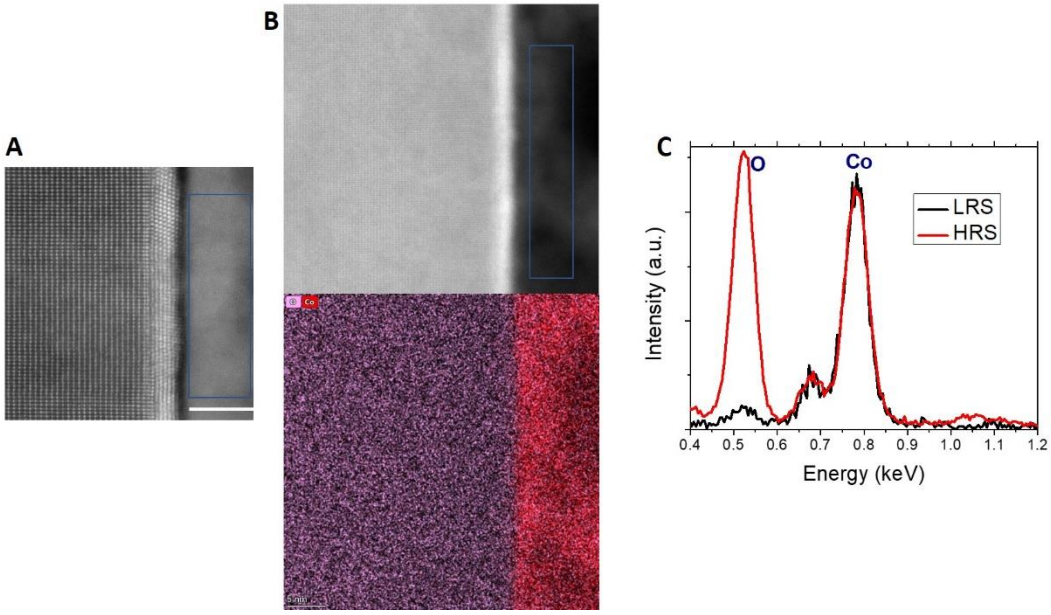

Chemical analysis of cycled tunnel junctions

A) Tunnel junction device in LRS from which EDS spectrum is obtained from the Co electrode region shown in blue box. B) Tunnel junction device (top) in HRS from which EDS spectrum is collected. (down) EDS map of Co and O, clearly showing Co rich and CoO_x rich regions in the top electrode. Scale bar, 5 nm for both (A) and (B). (C) EDS integrated spectra (normalized to Co L-edge), obtained from the blue boxed regions shown in (A) and (B). The HRS clearly has a large oxygen content and LRS has almost negligible content.

Fig. S8

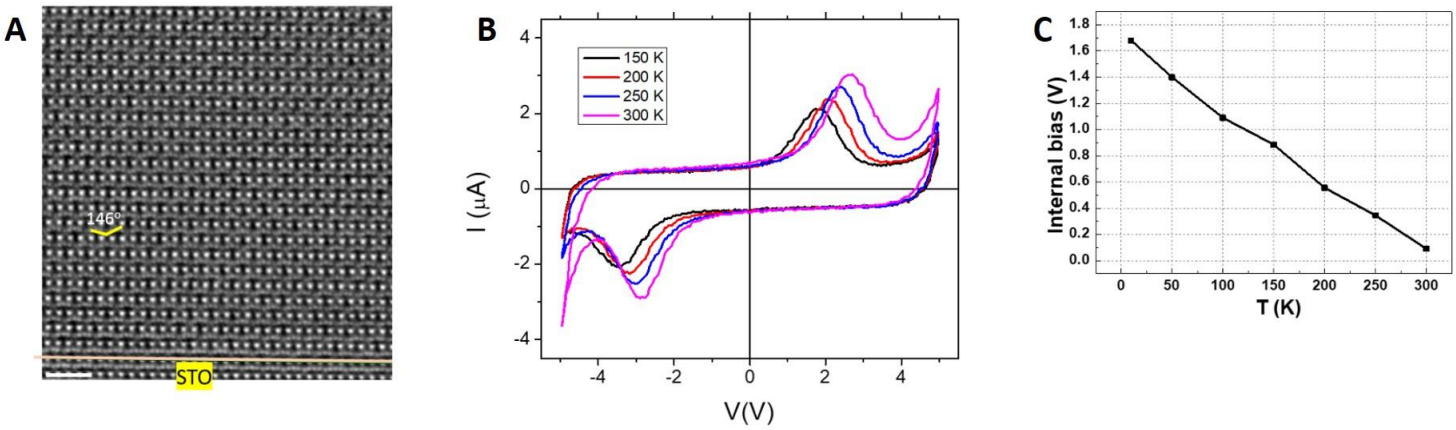

TiN/HZO/LSMO capacitors with temperature

(A) IDPC-STEM image of LSMO layer close to STO interface in the "down" polarized state of the TiN/HZO/LSMO device shown in Fig 4D and E of the manuscript. Note the exaggerated octahedral tilts. (B) I-V loops corresponding to the P-V loops presented in Fig. 4C of the manuscript. The $2P_r$ increases with increasing temperature, as shown in the inset of Fig. 4C. (C) Internal bias, calculated as $V_{c+}+V_{c-}$ as a function of temperature, where $V_{c+}(V_{c-})$ are coercive voltages under positive (negative) bias.

Fig. S9

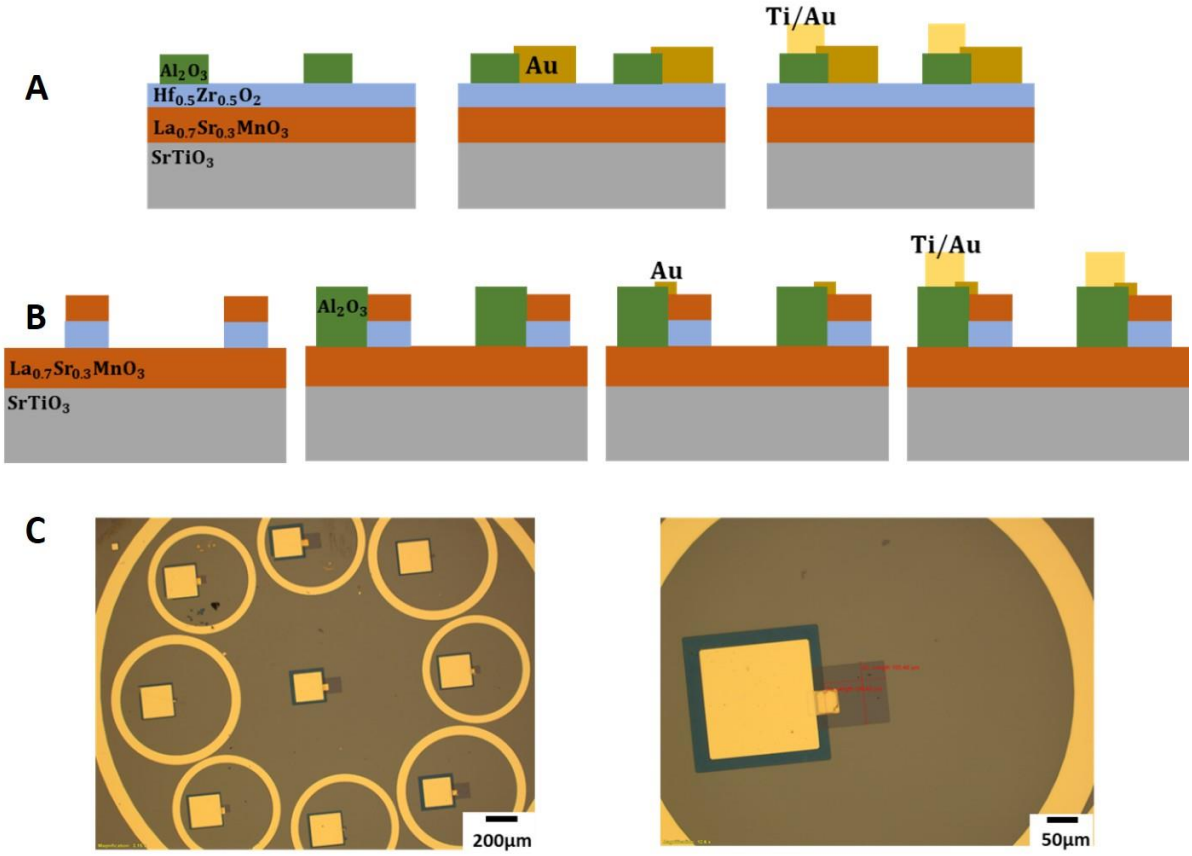

Device fabrication for the operando nanobeam synchrotron diffraction experiment:

(A) and (B) show the device fabrication process flow diagrams for the Au/HZO/LSMO and LSMO/HZO/LSMO capacitors, respectively. Standard photolithography techniques and e-beam evaporation were used. For the LSMO/HZO/LSMO devices etching was initially performed for the removal of top LSMO and HZO layers in order to pattern the devices of interest. Subsequently, for both type of capacitors, a thick layer of Al_2O_3 is used as the insulating base for a thick Ti/Au wire-bonding pad. The top electrodes (Au in (A) and LSMO in (B)) were electrically connected with the wire-bonding pad through partial overlapping in (A) and through the deposition of Au connecting layers in (B). The design of these devices preserves the electrical connectivity of the capacitors while their top surface remains optically free to be probed with the X-ray nanobeam. In (C), optical microscope images show the final shape of the LSMO/HZO/LSMO. Au rings were used during the alignment of the nanobeam.

Fig S10

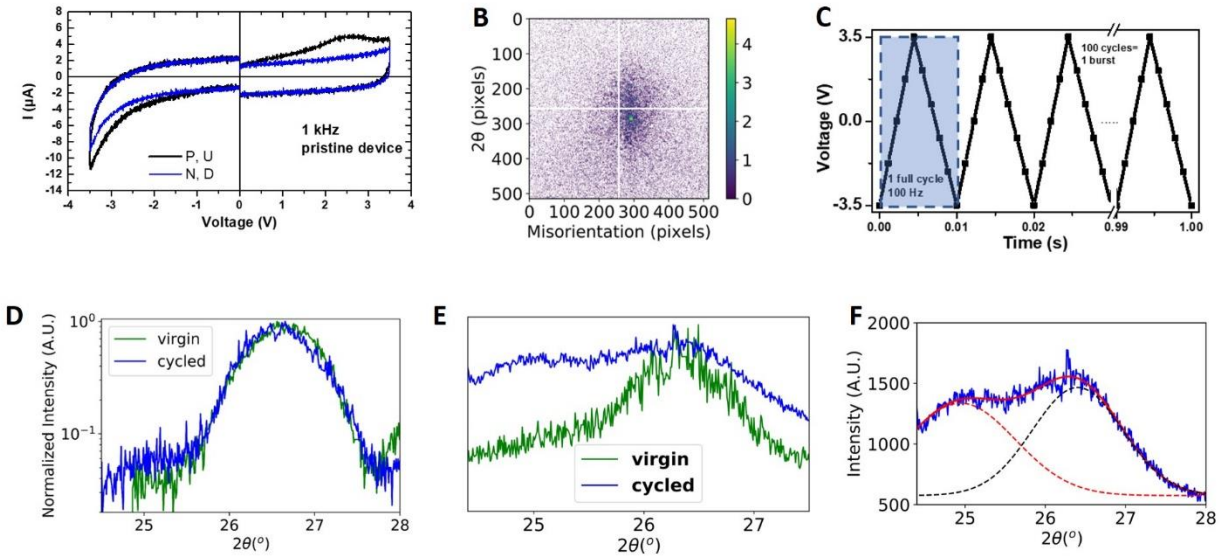

Operando nanobeam synchrotron diffraction results on Au/HZO/LSMO capacitors

A) I-V plots obtained from a PUND measurement on the Au/HZO/LSMO device tested in the Nanomax beamline (Max IV synchrotron, Lund, Sweden). B) Detector image at the Bragg peak position of HZO showing intense specular signal, and diffuse non-sepcular signal. C) 100 Hz biasing scheme used for the *operando* XRD measurements (the dots represent the 1 kHz measurement scheme used for dynamical measurements during cycling, not shown here). LSMO/HZO/LSMO and Au/HZO/LSMO capacitors were cycled for tens of thousands of times. D) 2θ projections of the 2D data obtained on LSMO/HZO/LSMO device before cycling (green) and after cycling showing no obvious changes. E) 2θ projection of the 2D data obtained on Au/HZO/LSMO device before cycling (green) and after cycling showing the appearance of a distinct peak related to a monoclinic phase with cycling. (F) Pseudo-voigt fits to data on cycled devices shown in (E).

Fig. S11

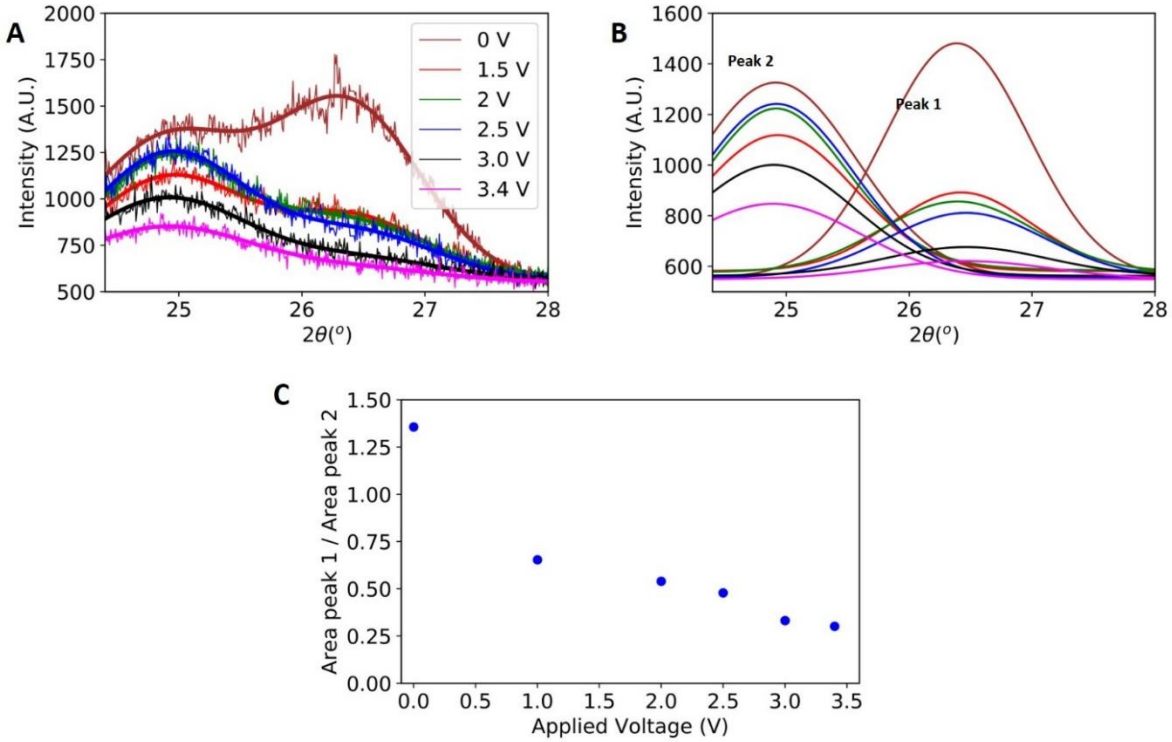

Phase analysis in HZO layer with positive DC bias in Au/HZO/LSMO capacitors:

2θ projections with DC bias on cycled Au/HZO/LSMO capacitor devices (A), the pseudo-Voigt fits of r-phase (right) and m-phase peaks (left) (B), and comparison of r/m peak intensities as a function of applied bias (C).

References:

49. U. Johansson, U. Voigt, A. Mikkelsen, NanoMAX : a hard x-ray beamline at MAX IV, *X-ray nanoimaging: instruments and methods* (2013), doi: 10.1117/12.2026609

50. A. Björling et al., Pytchographic characterization of coherent nanofocussed x-ray beam, Optics Express (2020), doi: 10.1364/OE386068

51. Z. Horita, T. Sano, M. Nemoto, Energydispersive x-ray microanalysis in the analytical electron microscope. *isij Int.* (1989), doi:10.2355/isijinternational.29.179.

52. F. P. G. Fengler, M. Pešić, S. Starschich, T. Schneller, C. Künneth, U. Böttger, H. Mulaosmanovic, T. Schenk, M. H. Park, R. Nigon, P. Muralt, T. Mikolajick, U. Schroeder, Domain Pinning: Comparison of Hafnia and PZT Based Ferroelectrics. *Adv. Electron. Mater.* (2017), doi:10.1002/aelm.201600505.